Oxidative Addition of Methane and Reductive Elimination of Ethane and Hydrogen on Surfaces: From Pure Metals to Single Atom Alloys

Tsuji, Yuta
Faculty of Engineering Sciences, Kyushu University

Yoshida, Masataka
Laboratory for Chemistry and Life Science, Tokyo Institute of Technology

Kamachi, Takashi
Department of Life, Environment and Applied Chemistry, Fukuoka Institute of Technology

Yoshizawa, Kazunari
Institute for Materials Chemistry and Engineering, Kyushu University

https://hdl.handle.net/2324/7160837

Oxidative Addition of Methane and Reductive Elimination of Ethane and Hydrogen on Surfaces: From Pure Metals to Single Atom Alloys

Yuta Tsuji,*[1] Masataka Yoshida,[2] Takashi Kamachi,[3] Kazunari Yoshizawa[4]

1. Faculty of Engineering Sciences, Kyushu University, Kasuga, Fukuoka, 816-8580, Japan
2. Laboratory for Chemistry and Life Science, Tokyo Institute of Technology, Midori-ku, Yokohama 226-8503, Japan.
3. Department of Life, Environment and Applied Chemistry, Fukuoka Institute of Technology, Higashi-ku, Fukuoka 811-0295, Japan
4. Institute for Materials Chemistry and Engineering, Kyushu University, Nishi-ku, Fukuoka 819-0395, Japan.
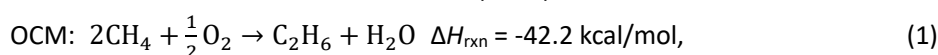
* To whom correspondence should be addressed.
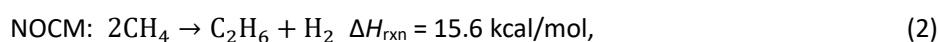E-mail: tsuji.yuta.955@m.kyushu-u.ac.jp

Abstract

Oxidative addition of CH_4 to the catalyst surface produces CH_3 and H. If the CH_3 species generated on the surface couple with each other, reductive elimination of C_2H_6 may be achieved. Similarly, H's could couple to form H_2. This is the outline of non-oxidative coupling of methane (NOCM). It is difficult to achieve this reaction on a typical Pt catalyst surface. This is because methane is over-oxidized and coking occurs. In this study, the authors approach this problem from a molecular aspect, relying on organometallic or complex chemistry concepts. Diagrams obtained by extending the concepts of the Walsh diagram to surface reactions are used extensively. C-H bond activation, i.e., oxidative addition, and C-C and H-H bond formation, i.e., reductive elimination, on metal catalyst surfaces are thoroughly discussed from the point of view of orbital theory. The density functional theory method for structural optimization and accurate energy calculations and the extended Hückel method for detailed analysis of crystal orbital changes and interactions play complementary roles. Limitations of monometallic catalysts are noted. Therefore, a rational design of single atom alloy (SAA) catalysts is attempted. As a result, the effectiveness of the Pt_1/Au(111) SAA catalyst for NOCM is theoretically proposed. On such an SAA surface, one would expect to find a single Pt monatomic site in a sea of inert Au atoms. This is desirable for both inhibiting over-oxidation and promoting reductive elimination.

1. Introduction

In recent years, it has been reported that reserves of methane-rich natural gas, such as tight gas, shale gas, and coalbed methane, are rapidly increasing.[1] Much research has been conducted to convert methane into useful chemicals, such as light alkanes, olefins, alcohols, and aromatic compounds.[2,3,4] Currently, indirect methods are most widely used for producing value-added products from methane: methane is partially oxidized or reformed to syngas (a mixture of CO and H_2), from which long-chain hydrocarbons and alcohols are produced by Fischer-Tropsch synthesis.[5,6] It would be of economic interest to evaluate the possibility of using natural gas as a feedstock for chemical synthesis.[7] Direct conversion of methane to light hydrocarbons by oxidative or non-oxidative coupling of methane (OCM or NOCM) has a potential for more efficient one-step methane upgrading, avoiding the energy-intensive syngas generation stage.[8,9] The primary products of OCM and NOCM, C_2 species (i.e., ethane or ethylene), are precursors to a variety of higher value chemical products, such as plastics and resins.[10] Using enthalpies of formation available in the literature,[11,12] the heat of reaction (ΔH_{rxn}) for each reaction is evaluated as follows:

OCM: $2CH_4 + \frac{1}{2}O_2 \rightarrow C_2H_6 + H_2O$ ΔH_{rxn} = -42.2 kcal/mol, (1)

and

NOCM: $2CH_4 \rightarrow C_2H_6 + H_2$ ΔH_{rxn} = 15.6 kcal/mol, (2)

where the product of OCM and NOCM is assumed to be ethane.

OCM was first reported in 1982,[13] and since then its study has been active worldwide.[14,15,16] The presence of an oxidant in OCM not only lowers the activation barrier for methane conversion, but also contributes to making the reaction thermodynamically favorable.[7,17,18] However, the formation of overoxidized species (CO or CO_2) is inevitable; improving the selectivity of C_2 formation in OCM has been a longstanding issue since the 1980s.[10] Although hundreds of catalyst candidates have been prepared and tested for OCM, the selectivity toward CO/CO_2 is typically about 50%, and the carbon utilization efficiency remains low.[19,20]

NOCM was first reported in 1991,[21] and since then its study has been active worldwide.[8,22,23] In NOCM, no oxidants are used, and production of undesirable CO_x species does not occur. In addition, hydrogen is co-produced as a valuable by-product.[24] The above points provide support for NOCM being more attractive than OCM in many cases. However, because no oxidant is used, the activation energy for methane conversion gets high compared to that in OCM, and the reaction is thermodynamically unfavorable. To achieve industrially important methane conversion rates (>10% conversion), reactions are typically performed at temperatures above 900 °C.[7,25,26] This results in high operating costs. But that is not the only problem. Coke formation is inevitable in reactions at such high temperatures and can lead to practical limitations, such as catalyst deactivation, process impairments, and loss of carbon yield.[7,27,28] To improve the NOCM reaction, great efforts have been made to find catalyst systems that work efficiently to activate the C-H bond of methane and promote C-C coupling, as well as to inhibit coking.[26,29,30,31,32,33,34]

According to the 1991 report by Belgued et al.,[21] continuous feeding of CH_4 to a 6 wt% Pt/SiO_2 catalyst at 250 °C yielded C_2H_6 and hydrogen. When the on-stream time exceeded 8 min, these products disappeared due to catalyst deactivation. Gerceker et al.[35] reported that the addition of Sn to Pt/SiO_2

increased the turnover frequency of ethylene formation by a factor of 3, and pretreatment of the catalyst at 850 °C reduced the extent of coke formation. Xiao et al.[10] reported that Pt-Bi bimetallic catalysts supported on ZSM-5 zeolite selectively converted methane to ethane with high carbon selectivity (>90%) and produced equimolar hydrogen as a by-product. The catalyst was hardly deactivated in an 8-hour test, indicating excellent stability and prevention of coke formation. We theoretically predicted that Pt-Mg bimetallic catalysts would be active for the NOCM reaction, working with experimentalists to validate our prediction by using a temperature-programmed-reaction under pure CH_4 gas stream.[34] The amount of carbon deposition on the Pt-Mg catalyst was found to be much lower than that on the Pt catalyst. These previous studies suggest that the NOCM reaction can be improved by adding another metal to Pt. The avoidance of coke formation observed on Pt surfaces is probably the most significant benefit of alloying Pt with other metals.[36,37]

CH_4 would be sequentially dehydrogenated on the Pt surface as $CH_4* \rightarrow CH_3* \rightarrow CH_2* \rightarrow CH* \rightarrow C*$,[38,39] where * indicates adsorbed species. Why cannot such reactions as the coupling of two CH_x species produced in this process to produce C_2H_{2x} and the coupling of CH_x and CH_y to produce C_2H_{x+y} occur? Of course, this is because the activation energy of each dehydrogenation step is lower than that of those coupling reactions.[34] If one performs first-principles calculations of the Pt surface, one can obtain fairly accurate energy profiles of the reactions, but we do not think that one can understand all of what is going on just by doing calculations ab initio.

Hoffmann and co-workers have revealed the low CO poisoning properties of Pt-Bi alloy surfaces by band calculations using the extended Hückel (eH) method.[40] They stated that the eH method does not allow geometrical optimization, nor is its energetics reliable, but it is transparent, and capable of explaining electronic effects. However, they also acknowledged that high-level calculations are necessary to confirm the qualitative picture of bonding and to provide accurate data about the energetics.[40] In fact, Hoffmann did just that in his collaboration with Nørskov et al. and succeeded in drawing a detailed picture of the bonding of H, C_2H_5, and CH_3 to the Pt(111) surface.[41]

Our goal in this paper is not to answer the question we raised above by bringing up the exact energy values obtained from density functional theory (DFT) calculations, but to provide a conceptual framework for understanding the phenomena using the eH method. And at the end of this paper, it will be shown that based on that concept, it is even possible to design a new catalyst logically, without relying on experience and intuition. The eH method was used very effectively in the studies by Tatsumi et al.[42] on reductive elimination of d^8 transition-metal complexes and by Saillard et al.[43] on activation of C-H and H-H bonds by transition-metal complexes. In this paper, we will do for metal surfaces what they have done for metal complexes using the eH method.

2. Theoretical Methods

2.1. DFT Calculations

It is essential to perform DFT calculations not only to obtain reliable adsorption structures of C_1 and C_2 species on the Pt surface but also to accurately evaluate the energetics of the methane

dehydrogenation process and the coupling reactions between C_1 species. We focus on orbitals at the surface because we aim to develop a qualitative concept to understand the reactions that occur on the surface. The orbitals are analyzed using the eH method as detailed in the next section.

We first optimized the face-centered cubic crystal structure of Pt. For this purpose, we used the periodic boundary DFT code of Vienna ab initio simulation package (VASP) 5.4.4.[44,45,46,47] The generalized gradient approximation was adopted with the functional described by Perdew, Burke, and Ernzerhof (PBE).[48] The Kohn–Sham equations were solved with a plane-wave basis set using the projector-augmented wave method.[49,50] The cutoff energy for the plane-wave basis set was set to 500 eV. The convergence threshold for self-consistent field iteration was set to 1.0×10^{-5} eV. The structure was relaxed until the forces on all of the atoms are less than 0.05 eV/Å. The Γ-centered k-point meshes with k spacing of $2\pi \times 0.05$ Å^{-1} were employed for sampling the Brillouin zone. Grimme's D3 dispersion correction formalism with Becke-Johnson damping[51] was adopted.

Based on the optimized bulk Pt structure detailed above, we constructed a slab model structure with a close-packed Pt(111)-(4 × 4) surface consisting of four atomic layers. A vacuum layer with a thickness of 15 Å was added on the surface. Using the slab model constructed, the adsorption structures of C_1 and C_2 species were optimized with VASP. The bottom two layers of the slab were kept fixed during the geometry optimization. The calculation conditions were set to be the same as those used for the bulk calculation mentioned above. Optimized surface structures shown in this paper were drawn by using VESTA.[52]

To obtain the transition-state structure and estimate the magnitude of the activation barrier for each reaction step, we performed climbing image-nudged elastic band calculations,[53,54,55] as implemented in VASP through the VTST Tools.[56] The spring constant between adjacent NEB images was set to 5.0 eV/Å^2. The number of NEB images (excluding the initial and final states) was set to four. The other calculation conditions were set to be the same as those used for the surface calculations mentioned above.

2.2. eH Calculations

In order to understand the origin of the activation energy of a reaction, it is very meaningful to examine the correlation between the orbitals of the reactant and those of the product. For this purpose, we draw orbital correlation diagrams by performing eH calculations. When Woodward and Hoffmann proposed the Woodward-Hoffmann rule, they applied the orbital correlation diagram to reactions of organic molecules.[57,58] Later, Hoffmann and co-workers extended the applicability of the diagram to chemical reactions of metal complexes.[42,43]

The orbital correlation diagram is also known as the Walsh diagram. It shows how one set of orbitals evolves into another set as a function of geometric change.[59,60] Although the energies of molecular orbitals (MOs) are usually used to construct the Walsh diagram, the target of our calculation in this study is not a molecule but an extended system, namely, the Pt surface, whose electronic structure should be described by using bands. In our previous work, we devised a method to draw a Walsh diagram for a surface by using the band energies calculated at the Γ point in the reciprocal space.[61] By using it, we analyzed the activation energy of the C-H bond cleavage reaction of methane on the IrO_2 surface. We apply that method

to the Pt surface in this paper. Walsh diagram analysis is suitable for tracing the continuous change of orbitals along the course of a reaction. On the other hand, if one wants to understand what orbital interactions are responsible for the important orbitals identified in the Walsh diagram, one can use the Crystal Orbital Hamilton Population (COHP)[62] analysis. It would be desirable to calculate the COHP at each point along the reaction coordinate and track the continuous changes in the shape of its spectrum.[63] However, the computational cost to achieve it would be high.

The image-dependent pair potentials (IDPP) method implemented in the QuantumATK 2021 package[64,65] was used to generate interpolated structures between the initial and final state structures of a reaction optimized with DFT calculations. For each interpolated structure, the eH method was used to calculate the energy levels of the bands at the Γ point. The Walsh diagram for a surface reaction was generated by plotting the energy levels continuously as a function of structural change.

In this study, eH calculations were performed using QuantumATK.[66] The first Brillouin zone was sampled using the Monkhorst-Pack method[67] with a 3 × 3 × 1 k-point mesh. Standard atomic parameters were taken from the literature[68] and are listed in Table S1 in the Supporting Information (SI). The off-diagonal matrix elements of the eH Hamiltonian were calculated using the approximation proposed by Hoffmann and co-workers.[69]

3. Results and Discussion

3.1. What Can We Learn from Surface Band Structure?

Let us start with the adsorption structure of methane on the Pt(111) surface (see Figure 1). Focusing on the coordination of CH_4 to Pt, the adsorption mode shown here is expressed in the terminology of complex chemistry as $\eta^3 - H, H, H$.[70] Other adsorption sites and coordination modes have been investigated in the literature,[71] but the energy difference between them is known to be very small.
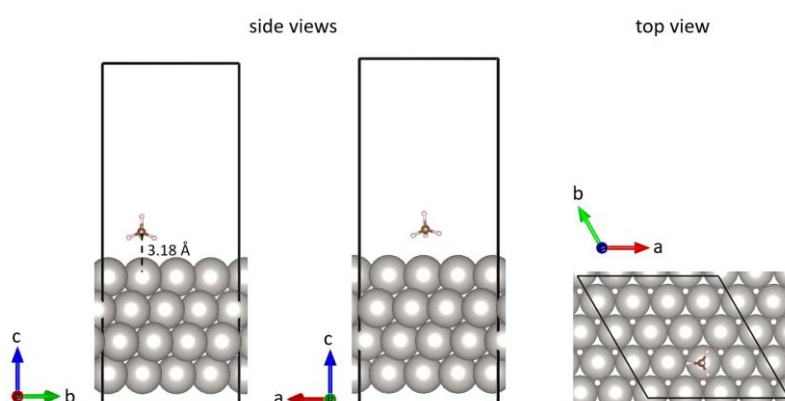

Figure 1. DFT-optimized adsorption structure of CH_4 on Pt(111) seen from three different angles. The black line represents the periodic boundary cell.

What can we say about the interaction of methane with the Pt surface in terms of orbital theory? The band structure calculated for the periodic boundary cell containing the methane adsorption structure

shown in Figure 1 is presented in Figure 2a. This band structure was calculated using the eH method. The Brillouin zone path used for this calculation is shown in Figure S1. It may be easy to infer that the energy region between -3 and 0 eV, where many bands are concentrated, corresponds to the d-band of Pt.
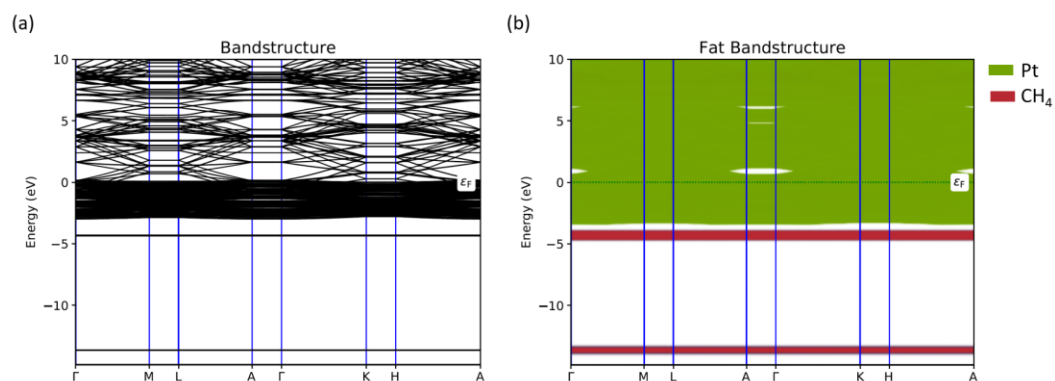

Figure 2. (a) eH-calculated band structure and fat band structure (green represents Pt orbitals and red represents CH_4 orbitals) calculated for the adsorption structure of CH_4 on Pt(111) shown in Figure 1. The Fermi level (ε_F) is taken as the point of zero energy.

It is a good idea to perform the fat band (projected band) analysis to understand the origin of the bands (see Figure 2b). The fat band analysis allows one to calculate the contribution of different orbitals to the band structure using the projection method. The bands dominated by the Pt orbital contribution are shown in green, while those dominated by the CH_4 orbital contribution are shown in red. By comparing Figures 2a and 2b, we can see that the flat bands at -4.3 eV and -13.7 eV are derived from the four σ_{C-H} orbitals (one a_1 and three-fold degenerate t_2 orbitals) of methane. The clear separation of the red and green regions indicates that the interaction between methane and the surface is very small. It is not possible to determine from these figures which bands are responsible for the reaction of methane on the surface.

3.2. Analysis of the Reactions of Methane on Pt Surface with DFT Calculations

In the present study, we first performed DFT calculations to get a rough idea of the reaction of methane on the Pt surface. We then studied the orbital interactions at the surface in detail. We shall begin with the structures and energy profiles of the dehydrogenation of methane on Pt(111).

Figure 3 shows the energy profile for each step of the dehydrogenation of CH_4 to CH via CH_3 and CH_2 on Pt(111). This series of methane activation processes is what is called oxidative addition in the field of organometallic chemistry. The activation energies for the cleavage of the first two C-H bonds of methane are comparable, and that of the third C-H bond is much smaller, less than half that of the first two. This trend is in good agreement with the trend reported in preceding theoretical calculations.[34,72] If the first activation barrier can be overcome, it is expected that the subsequent activation barriers can also be overcome. Thus, these potential energy diagrams suggest that it is very difficult to stop the over-oxidation of methane on the Pt surface.
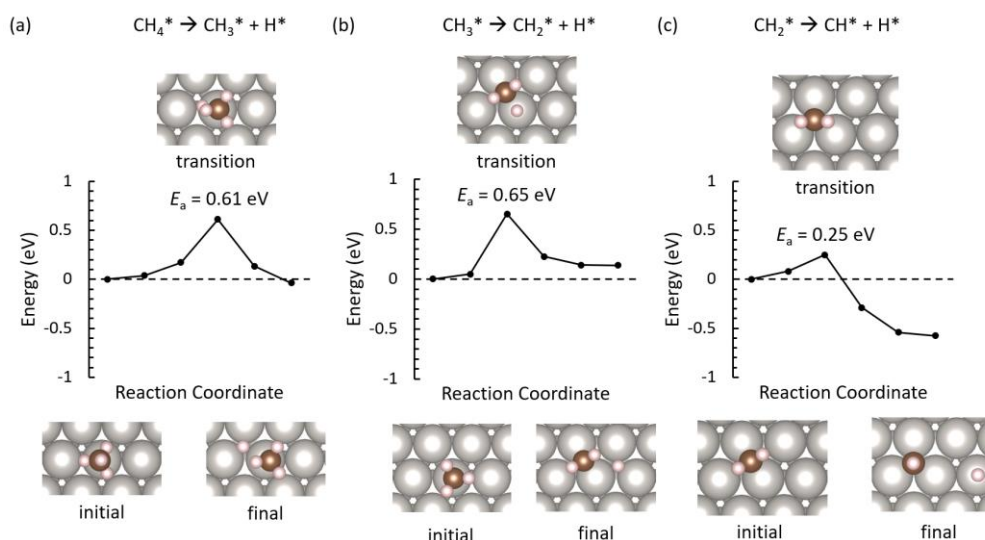
Figure 3. Energy profiles for methane dehydrogenation on Pt(111) calculated at the DFT level: (a) $CH_4^* \rightarrow CH_3^*$ + H^*, (b) $CH_3^* \rightarrow CH_2^*$ + H^*, and (c) $CH_2^* \rightarrow CH^*$ + H^*, where * denotes an adsorbed species. Top views of the initial, transition, and final state structures are shown. Each dot in the energy profiles corresponds to each NEB image. In each step, the energy of the initial state is set to the zero energy. The activation barrier of each reaction (E_a) is indicated.

We hope that two CH_3^* and two H^* species would couple to produce C_2H_6 and H_2, respectively. However, the energy diagrams shown in Figure 4 imply that this would not happen. The reaction coordinates for these reactions were determined from those given in the literature.[59,73,74,75] The activation barrier for the H-H coupling is about 1 eV, and that for the C-C coupling is even higher, about 2.6 eV. Thus, the dehydrogenation of CH_3 is preferred over the C-C coupling. Why is it so hard to form the C-C bond on the Pt surface?
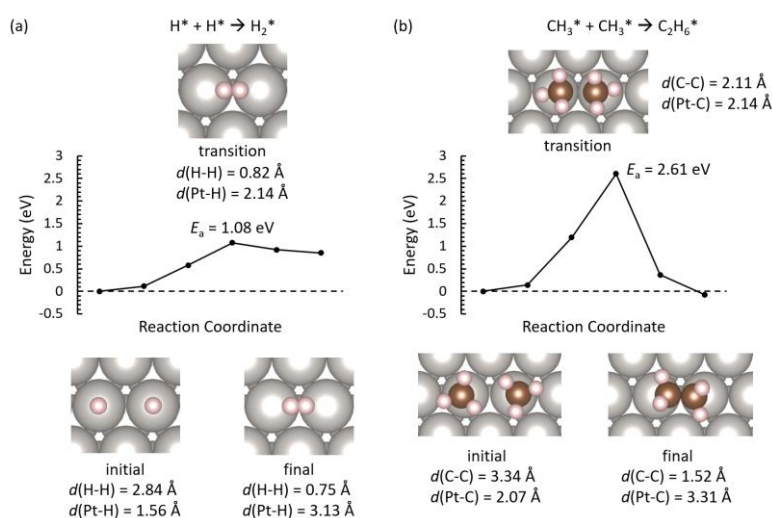

Figure 4. Energy profiles for H-H and C-C coupling reactions on Pt(111) calculated at the DFT level: (a) H^* + $H^* \rightarrow H_2^*$ and (b) CH_3^* + $CH_3^* \rightarrow C_2H_6^*$. In each structure, the nearest neighbor H-H, Pt-H, C-C, and Pt-C interatomic

distances are shown.

Reductive elimination of an alkane from a transition metal center is a common organometallic reaction as shown in Figure 5, occurring for a wide range of metals, coordination numbers and geometries, and ligands.[76] This reaction is efficiently accomplished by d^8 transition metal centers such as Ni(II), Pt(II), Pd(II), and Au(III).[76] This fact underscores the difference between metal complexes and surfaces. The difference in the oxidation state of the Pt atom on the surface and that in the complex seems to be responsible for the difference in reactivity.
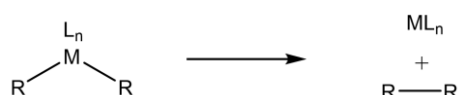
Figure 5. Coupling of two coordinated alkyl groups (R) into an alkane, where M and L denote the metal center and a ligand, respectively.

States in the surface layer have somewhat less band dispersion, i.e., form narrower bands due to the fact that the surface atoms have fewer nearest neighbors, so charge transfer to the surface from the bulk occurs at the right side of the transition series.[43] Such a surface should be negative relative to the bulk. Thus, the electronic population on the Pt surface is likely to prohibit the coupling reaction. We give advance notice that a more clear explanation with eH calculations will be presented at a later part of this manuscript.

We are discouraged by the large activation energy shown in Figure 4b. Nevertheless, since it is known that in Fischer-Tropsch synthesis,[77] C-C bonds are formed on metal catalyst surfaces and the carbon chain becomes longer and longer, we decided to refer to this reaction mechanism. Although the full extent of this reaction has not yet been elucidated, one of the leading proposals is the carbide mechanism.[78,79] According to it, CH_3^* and CH_2^* react to form $C_2H_5^*$ as an important intermediate. We have calculated the energy profile of the process of ethane formation via $C_2H_5^*$ on the Pt(111) surface, as shown in Figure S2. The activation barrier for C-C coupling has been reduced to 0.79 eV; the activation energy for the hydrogenation of $C_2H_5^*$ to form $C_2H_6^*$ is smaller, 0.57 eV. Thus, if the activation barrier for the reaction of $CH_2^* \rightarrow CH^* + H^*$ were higher than that of $CH_2^* + CH_3^* \rightarrow C_2H_5^*$, ethane could be formed on the Pt surface. However, the reality is that this is not the case; coking is doomed to occur on the Pt surface, as experiments show.[10,34]

3.3. Rationalization of Reaction Barriers Based on Orbital Analysis Using eH Calculations

DFT calculations provide a very reliable potential energy diagram, so one can easily guess what will happen on the surface. Based on this, one can justify experimental results. However, it is difficult for theory to reach beyond experiment. A conceptual framework for understanding reactivity is needed. Once such a framework is established, one can speculate on systems that have not yet been tested. We believe we can do that with qualitative eH calculations, the results of which are presented below.

Let us start with C-H activation. Using the structures of the initial and final states shown in Figure

3a with the Pt atoms removed and the IDPP interpolated structures between them, we obtained a Walsh diagram corresponding to the process of the elongation of a C-H bond of methane in the absence of the catalyst. This calculation was done at the eH level, resulting in Figure 6. The symmetry lowering associated with the structural deformation leads to the lifting of the three-fold degeneracy of the methane highest occupied molecular orbitals (HOMOs). One of the HOMOs has a large amplitude on the C-H bond that is being broken, so its energy increases as the reaction proceeds. On the other hand, as for the lowest unoccupied molecular orbital (LUMO), the energy decreases rapidly as the reaction proceeds. In this orbital, a node of the wave function is observed on the C-H bond. The LUMO descending is due to its C-H antibonding (σ_{C-H}^*) character, while the HOMO ascending is due to its C-H bonding (σ_{C-H}) character. It should be noted that we are using the eH method to calculate a closed shell configuration, so the electronic state in the dissociation limit cannot be correctly described.
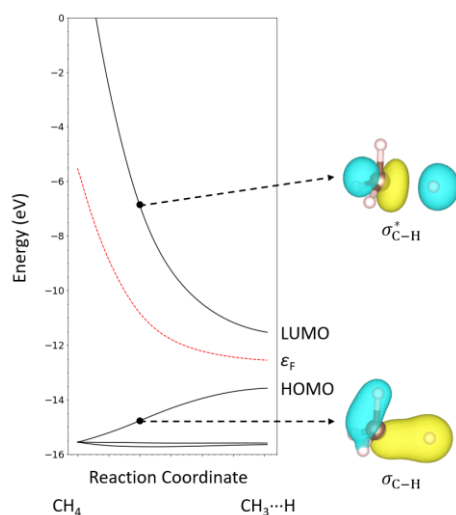

Figure 6. Walsh diagram at the eH level for the elongation of a C-H bond of methane with the shape of the HOMO and LUMO at a point along the reaction coordinate. The red dashed line indicates the Fermi level of the molecule. The vacuum level is defined as zero energy.

During this reaction process, the total energy of the system is only increasing. This corresponds to the fact that the HOMO energy continues to rise. No matter how much the energy of the LUMO decreases, as long as it is not occupied by electrons, the change in its orbital energy does not affect the energy of the whole system. How does the Walsh diagram shown in Figure 6 change when the C-H bond is broken with the molecule interacting with the Pt surface? That is what we shall look at below.

Figure 6 was obtained by tracking the MO energy changes. However, the methane molecule interacting with the Pt surface is no longer an isolated molecular system but an extended system, so its electronic structure is described by bands, i.e., crystal orbitals. Therefore, we decided to use their energy levels, which are functions of the coordinates in reciprocal space. We chose the Γ point and calculated the energy levels at that point. There are some examples in the literature where Walsh diagrams were used to analyze surface reactions. [61,80] These studies revealed that the choice of the reciprocal space point has little

effect on the shape of the resultant diagram.

Figure 7a shows a Walsh diagram calculated for the C-H bond cleavage reaction of methane on the Pt surface. A dense region of energy levels is found in the -14 to -11 eV range. Those levels are the d-band of Pt. Their energies change little as the reaction proceeds. This implies that they are not involved in the reaction. There are many flat levels in the region above the Fermi level. Their involvement in the reaction will be negligible. On the other hand, one can see an energy level falling down from the upper left. When that level crosses the flat levels, there are avoided crossings. Orbital mixing may easily occur because of the low symmetry nature of the surface system. Below the Fermi level, a level is seen to rise from around -15.5 eV as the reaction proceeds.

The large number of levels makes Figure 7a difficult to read, so a crafted version is shown in Figure 7b, in which the gradient of each energy level is calculated and the energy levels are displayed only when the gradient is greater than 0.1 eV/Å. Interestingly, the unit of the gradient is the same as that of force. We could call it orbital force.[81,82] By looking at this figure, one would be able to clearly recognize the state of descent from the upper left and the state of ascent from the lower left. Those states would correspond to the σ^*_{C-H} and σ_{C-H} orbitals shown in Figure 6. The distributions of crystal orbitals calculated for the states in the initial stage of the reaction shown in Figure 7b justify this correspondence.
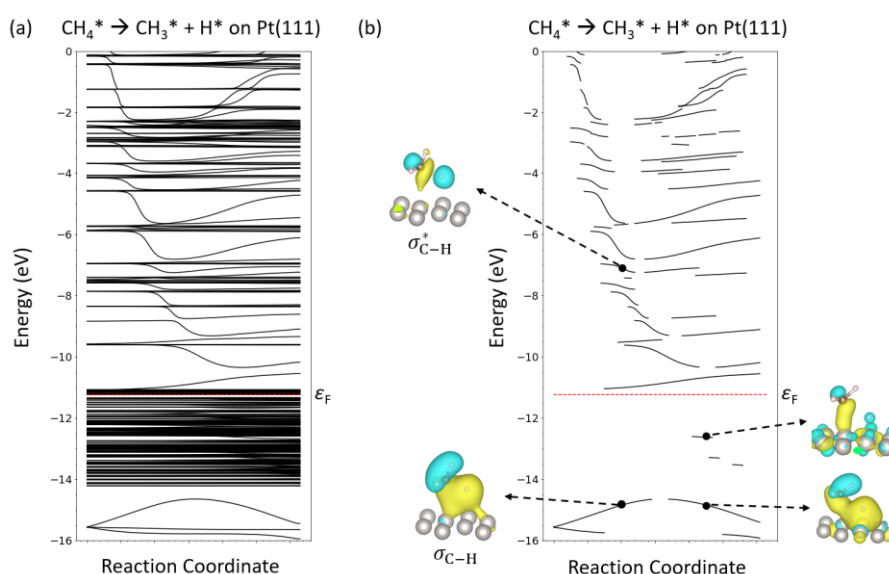

Figure 7. (a) eH-calculated evolution of the crystal orbital levels calculated at the Γ point along the reaction coordinate for the first C–H bond cleavage reaction of methane on the Pt surface. (b) Plots obtained by extracting the portion of the curves in (a) whose gradients are greater than 0.1 eV/Å. Selected Γ-point crystal orbital distributions are visualized with an isovalue of 0.03 bohr^{-3}.

In the Walsh diagram shown in Figure 7b, one will notice that the way the σ_{C-H} and σ^*_{C-H} orbitals change differs from that shown in Figure 6 in the second half of the reaction. The energy of the σ_{C-H} orbital begins to drop and the σ^*_{C-H} orbital drops to an energy below the Fermi level. The crystal orbital distributions of these levels are also shown in Figure 7b, and it becomes clear why their energies

drop: they are in a bonding interaction with the surface orbitals.

In the initial stage of the reaction, the energy of the σ_{C-H} orbital increases due to the elongation of the C-H bond. At this stage, since the molecule is far from the surface, the bonding interaction with the surface is not sufficient and destabilization prevails. It would be reasonable to relate such a destabilization effect to the origin of the activation energy. In the second half of the reaction, the bonding interaction between the surface and the molecule prevails and the energy of the σ_{C-H} orbital begins to decrease. Furthermore, the σ_{C-H}^{*} orbital gets occupied by electrons as it drops below the Fermi level due to the bonding interaction with the surface. The decrease in energy of these two states will have an important impact on the stabilization of the system.

It is possible to create a Walsh diagram for the same reaction using the DFT method, which is actually shown in Figure S3. From that, one can only draw essentially the same conclusion as drawn from the one generated using the eH method. Therefore, still, in view of the computational cost required for DFT calculations, we will continue to rely on the eH method to generate Walsh diagrams in this paper.

Drawing the Walsh diagram allows for a reasonable, albeit qualitative, explanation of the origin of the activation barrier. Our attempt to use this technique to understand the height of the activation barriers for the reactions shown in Figure 4 is described below. Let us begin with the Walsh diagram in the absence of the catalyst (see Figure 8). In the gas phase, reactions in which H radicals couple to form H_2 and CH_3 radicals couple to form C_2H_6 occur without barriers.[83] The Walsh diagrams shown in Figure 8 support this: as the reaction proceeds, the bonding orbital between the hydrogen atoms and that between the carbon atoms, corresponding to the HOMOs of the H_2 and C_2H_6 molecules, get more and more stable. This corresponds to the reaction proceeding without a barrier. The LUMOs, corresponding to the antibonding orbitals, only increase in energy, but since no electrons are involved, the energy change in the system will not be affected. The reason why the HOMO and LUMO are almost equal in energy on the left side of these Walsh diagrams is that the electronic state for the radicals is calculated as a closed shell configuration. This is a weakness of the eH method. Care must be taken in interpreting such an electronic state. By contrast, one can trust the MO level diagram calculated with the eH method when the HOMO-LUMO gap is large.
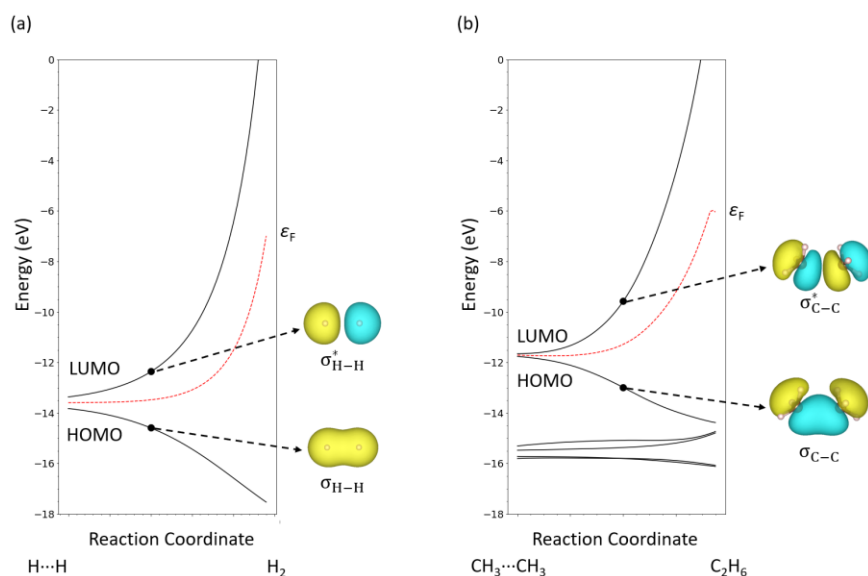
Figure 8. Walsh diagrams at the eH level for the gas phase reactions of (a) H + H $\rightarrow$ H$_2$ and (b) CH$_3$ + CH$_3$ $\rightarrow$ C$_2$H$_6$ with the shape of the HOMO and LUMO at a point along the reaction coordinate.

In Figure 8b, two ascending and two descending orbitals can be seen in the energy region below the HOMO. It is worthwhile to look at the ethane MOs to better understand the nature of these orbitals. Figure 9 shows how the interaction between the orbitals of two pyramidal CH$_3$ fragments leads to the MOs of staggered C$_2$H$_6$ depicted on the right-hand side of Figure 9.[59] For simplicity, the C-H antibonding orbitals of CH$_3$ are not included in this figure. On the left side of the figure are the 1a$_1$, 1e, and 2a$_1$ orbitals of the pyramidal CH$_3$ fragment with C$_{3v}$ symmetry, denoted as σ_s, $\pi_{x(y)}$, and n$_\sigma$, respectively. As a first approximation, one only needs to apply degenerate perturbation theory to the MOs of two CH$_3$'s to obtain those of C$_2$H$_6$, just taking positive and negative—bonding and antibonding—combinations. The 1a$_{1g}$ and 1a$_{2u}$ MOs are primarily in-phase and out-of-phase combinations of the two σ_s fragment orbitals, denoted as σ_s^+ and σ_s^-, respectively. Similarly, the in-phase and out-of-phase combinations of the two n$_\sigma$ fragment orbitals give rise to the 2a$_{1g}$ and 2a$_{2u}$ MOs, denoted as σ and σ*, respectively. The $\pi_{x(y)}^+$ and $\pi_{x(y)}^-$ MOs (e$_u$ and e$_g$, respectively) are generated from the two $\pi_{x(y)}$ MOs.
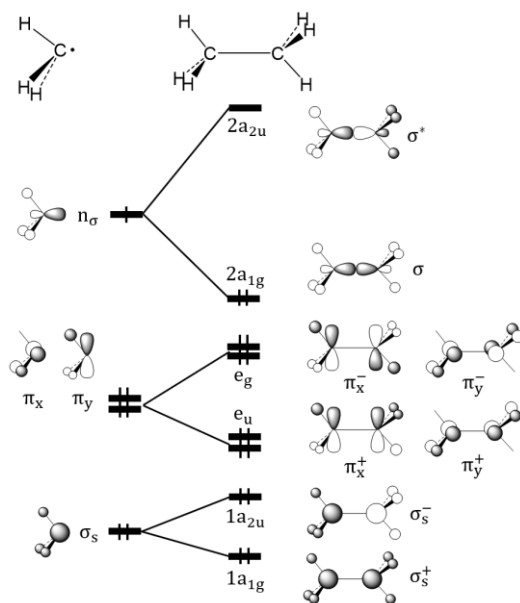
Figure 9. Construction of the MOs of staggered C_2H_6 in terms of the orbitals of two pyramidal CH_3 fragments.

Comparing Figure 8b with Figure 9, the four MOs in the -16 to -15 eV range are identified as $\pi_{x(y)}^+$ and $\pi_{x(y)}^-$. As is clear from Figure 9, the destabilization of σ_s^- and $\pi_{x(y)}^-$ associated with the C-C bond formation can be compensated by the stabilization of σ_s^+ and $\pi_{x(y)}^+$, respectively. That is why the σ ($2a_{1g}$) orbital is important when discussing the energy change of the system.

Let us see how the Walsh diagram in Figure 8a is perturbed by the Pt surface. Figure 4a suggests that the two Pt atoms immediately below the H atoms seem to be particularly important for the reaction. Thus, we start with the cluster model of Pt_2H_2 consisting of those two Pt and two H atoms. This cluster model is a cutout of the corresponding part of the slab model shown in Figure 4a, so the bond lengths are the same as those in the slab model. Nakatsuji et al.[84] also used a similar model to study the dissociative adsorption of H_2 on the Pt surface and reported the results of their detailed study in terms of orbital interactions and electron correlation.

Figure 10 shows a Walsh diagram for the reaction of H + H → H_2 on the Pt surface, which is boldly modeled with the Pt_2 cluster. Although just two Pt atoms have been added, Figure 10 looks much more complicated than Figure 8a. Importantly, however, as the reaction progresses, the energy of the σ_{H-H} orbital descends, while the σ_{H-H}^* orbital rises, scraping through many orbitals. From this perspective, Figure 10 has much in common with Figure 8a. As Woodward and Hoffmann analyzed a series of organic reactions,[57] we shall draw a more abstract correlation diagram based on Figure 10 to further discuss this reaction.
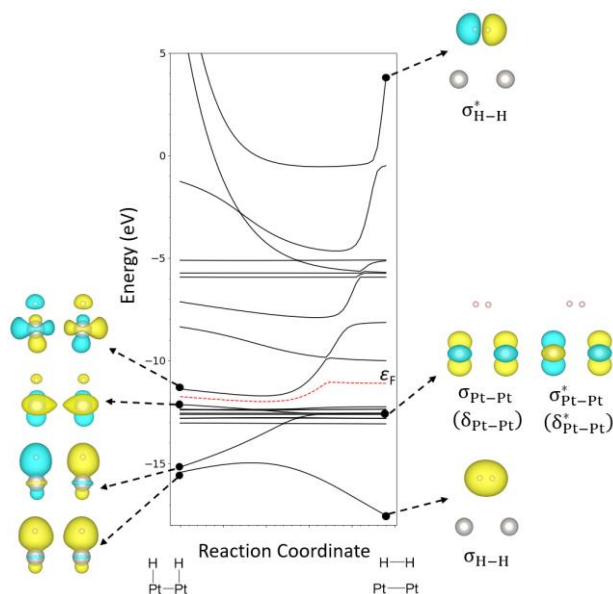
Figure 10. Walsh diagram at the eH level for H + H $\rightarrow$ H$_2$ in the Pt$_2$H$_2$ cluster model. The MOs consisting of the d$_{z2}$ orbitals of the Pt atoms in the product are labeled as σ and σ*. Some may object to this classification and prefer to call them δ and δ*.[84] Actually, the classification of these orbitals is very difficult because the bond and z axes are different in this case.

The mirror plane perpendicular to the Pt-Pt and H-H bonds is a symmetry element imposed by the geometry of the Pt$_2$H$_2$ system and the orbitals shown in Figure 11 are either symmetric (S) or antisymmetric (A) with respect to that element. Levels of like symmetry have to be connected, paying due attention to the quantum mechanical non-crossing rule.[57] The lower A orbital in the reactant (σ^*_{Pt-Pt} + σ^*_{H-H}) wants to correlate to the σ^*_{H-H} orbital, i.e., the higher A orbital in the product, but the level crossing is impossible. Instead, it correlates to the σ^*_{Pt-Pt} orbital.

Figure 11 shows that the σ^*_{Pt-Pt} + σ^*_{H-H} orbital, which is occupied, has to soar to high energy to reach the transition state due to its correlation to the higher-lying σ^*_{H-H} orbital. This rationalizes that the activation energy for the reductive elimination of H$_2$ from the Pt surface is relatively large. Trinquier and Hoffmann[85] thoroughly investigated the reductive elimination of H$_2$ from dinuclear complexes. The Walsh diagrams they drew are similar to the ones we see here. A difference would be that they were looking at discrete isolated molecules while we are looking at a portion of the surface that is an extended system.
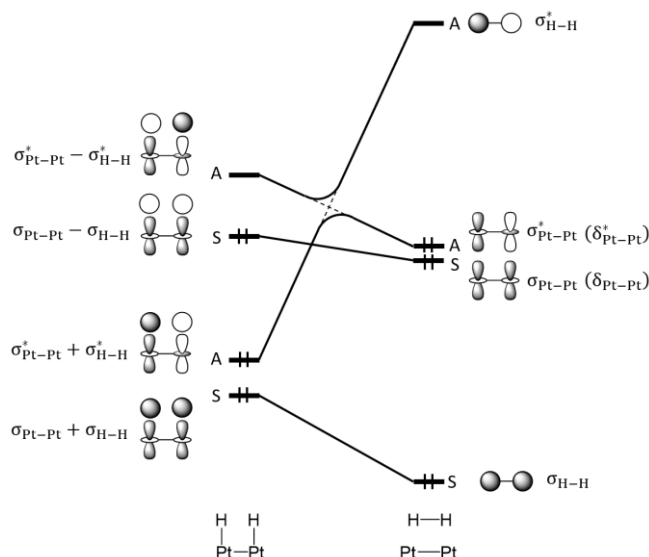
Figure 11. Correlation diagram for the reductive elimination of H_2 from the Pt_2H_2 cluster. The orbitals are labeled using S or A, which denotes whether the orbital is symmetric (S) or antisymmetric (A) with respect to the mirror plane perpendicular to the Pt-Pt and H-H bonds.

A Walsh diagram for the H-H coupling on the Pt surface is shown in Figure 12a. One will perceive that this figure is essentially the same as Figure 10, although many levels are shown due to the large number of atoms in the unit cell. A figure obtained by eliminating flat orbital levels is shown in Figure 12b. Several crystal orbital distributions are also shown. They are named with the same labels used in Figure 11 so that one can realize a one-to-one correspondence between them and the MOs schematically shown in Figure 11. As the reaction progresses, the σ_{H-H}^* orbital is seen to soar, avoiding crossing with many levels.
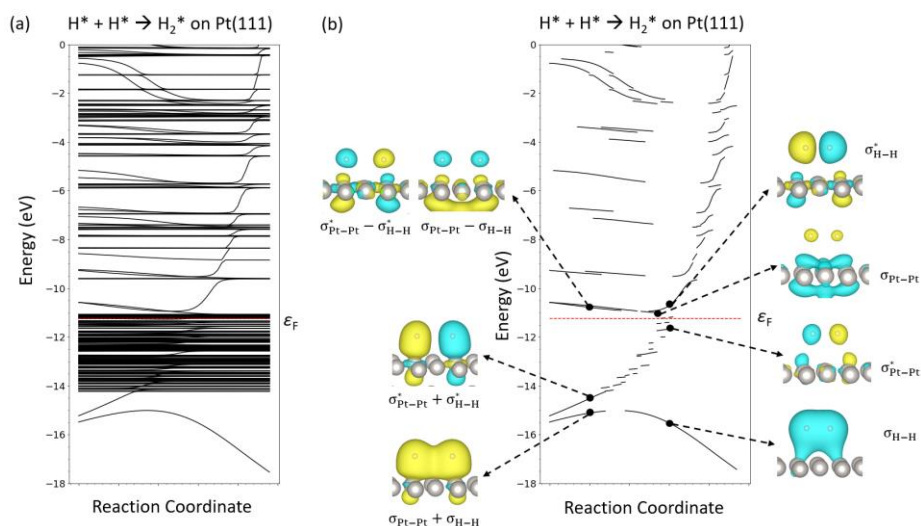

Figure 12. (a) eH-calculated evolution of the crystal orbital levels calculated at the Γ point along the reaction coordinate for H* + H* → H_2* on the Pt surface. (b) Plots obtained by extracting the portion of the curves in (a) whose gradients are greater than 0.2 eV/Å. Selected Γ-point crystal orbital distributions at points along the reaction coordinate are visualized with an isovalue of 0.03 bohr^{-3}.

15

In the initial stage of the reaction, the $\sigma^*_{Pt-Pt} + \sigma^*_{H-H}$ orbital contains electrons, and the destabilization of the system due to the increase in energy of this orbital is likely to be the origin of the activation barrier. To some extent, this destabilization is mitigated by the stabilization of the $\sigma_{Pt-Pt} + \sigma_{H-H}$ orbital. In the second half of the reaction, the $\sigma^*_{Pt-Pt} + \sigma^*_{H-H}$ orbital gets located above the Fermi level, and the electrons in the orbital flow out of it. Thereafter, this orbital turns into the σ^*_{H-H} orbital and destabilization is not a problem any longer.

Let us investigate the origin of the very high activation barrier of the C-C coupling reaction in Figure 4b. Since we already have a good understanding of the origin of the activation barrier to the H-H σ bond formation, we can understand the C-C σ bond formation within the same framework. The reader should now be able to draw the C-C coupling version of the correlation diagram as in Figure 11. So we skip the cluster model and look at the Walsh diagram computed for the slab model as shown in Figure 13. As the reaction progresses, the $\sigma^*_{Pt-Pt} + \pi^*_{C-C}$ orbital rises from around -14 eV through many avoided crossings.
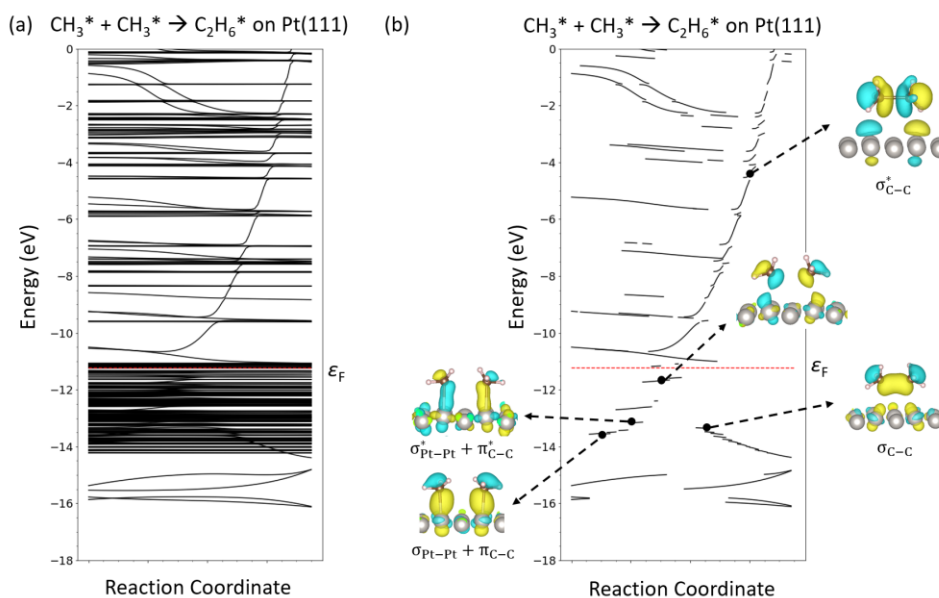

Figure 13. (a) eH-calculated evolution of the crystal orbital levels calculated at the Γ point along the reaction coordinate for $CH_3^* + CH_3^* \rightarrow C_2H_6^*$ on the Pt surface. (b) Plots obtained by extracting the portion of the curves in (a) whose gradients are greater than 0.1 eV/Å. Selected Γ-point crystal orbital distributions at points along the reaction coordinate are visualized with an isovalue of 0.03 bohr^{-3}.

Figure 13 shows how the $\sigma^*_{Pt-Pt} + \pi^*_{C-C}$ orbital continues to rise with electrons in the early stages of the reaction. When the orbital reaches the Fermi level, the electrons are transferred to empty levels. This occurs near the transition state. The $\sigma^*_{Pt-Pt} + \pi^*_{C-C}$ orbital emptied continues to rise, changing to the σ^*_{C-C} orbital, but since there are no electrons any more in the orbital, its energy increase does not destabilize the system. The energy cost of the $\sigma^*_{Pt-Pt} + \pi^*_{C-C}$ orbital pushing the electrons up to the Fermi level is the main origin of the activation barrier in this reaction.

3.4. What Can Be Done to Lower the Activation Barrier for C-C Coupling Reaction on Pt Surfaces?

If the work function of the surface were larger, the $\sigma^*_{Pt-Pt} + \pi^*_{C-C}$ orbital would reach the Fermi level earlier. The activation energy would be smaller. Alternatively, if the energy of the $\sigma^*_{Pt-Pt} + \pi^*_{C-C}$ orbital at the beginning of the reaction were higher, the energy cost of bringing it to the Fermi level would be smaller. Such a situation might be realized if the Pt-Pt antibonding interaction were stronger, or if the Pt-C bonding interaction were weaker. The latter is particularly intuitive. In short, the barrier would be smaller if the Pt-C bond were weaker.

Perturbing the strength of the bond is interesting but difficult; we would like to explore ways to do so in the future. On the other hand, lowering the Fermi level might be more easily achieved. Experimentally, it would be possible to achieve that by applying a positive bias to the surface. Computationally, it could be accomplished by reducing the total number of electrons in the unit cell. VASP allows the calculation of such a charged unit cell by adding a compensating uniform background charge.[86,87] This is a generally accepted method used for a variety of purposes.[88,89]

The decrease in the total number of electrons in the unit cell lowers the Fermi level as shown in Figure 14a. The corresponding decrease in the activation energy of the C-C coupling reaction is shown in Figure 14b. We obtained this figure by performing NEB calculations of the C-C coupling reaction in charged cells. As the unit cell charge increases, the Fermi level decreases and the $\sigma^*_{Pt-Pt} + \pi^*_{C-C}$ orbital can reach the Fermi level at an earlier stage and the activation energy decreases. This means that the structure reaches the transition state earlier. Based on Hammond's postulate,[90] the transition state is expected to become more similar to the structure of the reactant. We can confirm that this is indeed the case: As the activation energy decreases, the C-C bond in the transition state stretches while the Pt-C bond shrinks. As for the heat of reaction, it seems to depend little on the charge of the unit cell (see Figure S5). We have shown that it is possible to lower the activation energy of C-C coupling by lowering the Fermi level. However, the extent of the reduction of the activation barrier is limited, and the activation barrier for C-C coupling is still high. That is why over-oxidation will be preferred on the Pt surface (the effect of the Fermi level lowering on the over-oxidation is detailed in Figure S6).
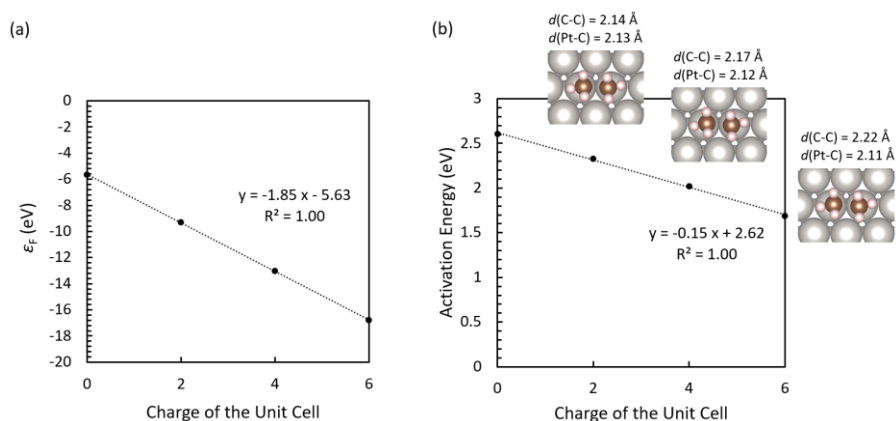

Figure 14. (a) How the Fermi level (ε_F) with reference to the vacuum level and (b) the activation energy of the C-C coupling change as the unit cell charge increases. These calculations were done at the DFT level. The structure of the transition state is shown as an inset. The regression lines and the corresponding R^2 values are shown.

Now that we understand the effect of the change in the Fermi level of the Pt surface on the activation barrier for the C-C coupling, the reader may be interested in the effect of the Fermi level change on the activation barrier for the first C-H bond breaking reaction in methane. Figures S7a and S7b show how the activation energy and heat of reaction change as the unit cell charge changes, respectively. The relationship between the activation energy and the heat of reaction is shown in Figure S7c. The clear linear relationship between the charge of the unit cell and the activation energy, as seen in Figure 14b, is not seen in Figure S7a. This suggests that the effect of the Fermi level change on the activation energy of the C-H bond cleavage is not simple.

Looking closely at Figure S7a, one can see a region where the activation energy decreases as the Fermi level decreases and a region where the activation energy increases as the Fermi level decreases. Figure S7b shows that the same is true for the heat of reaction. This suggests that two opposing mechanisms are at work. To find out what they are, we analyzed the COHP[62] for the C-H bond that is about to be broken in the transition state structure shown in Figure 3a. To this end, we analyzed the wave function output by VASP using LOBSTER v4.1.0.[91,92,93] The COHP spectrum so obtained is shown in Figure 15a. Here, the COHP values are multiplied by -1, so positive values correspond to bonding interactions while negative values correspond to antibonding interactions.

We note three small peaks near the Fermi level in Figure 15a. The two peaks below the Fermi level exhibit a C-H antibonding character, while the one above the Fermi level exhibits a C-H bonding character. Thus, one can see that the higher energy one is derived from the σ_{C-H} orbital while the lower energy ones are derived from the σ_{C-H}^*. This is also supported by the partial charge density maps. In the maps, one can also see that the interaction between the σ_{C-H} orbital and the surface orbitals is antibonding, while that between the σ_{C-H}^* orbital and the surface orbitals is bonding. Based on these observations, we can draw an orbital interaction diagram between the surface and methane, as shown in Figure 15b.

Figure 15b clearly shows two factors governing the C-H bond activation of methane on the Pt surface: one is the charge transfer from the Pt d-band to the σ_{C-H}^* orbital (see the orbitals in blue); the other is the charge transfer from the σ_{C-H} orbital to the d-band (see the orbitals in orange). Note that the orbital interaction between occupied and empty orbitals results in a charge transfer from the occupied to the empty.[94] The orbital with the energy of about -12.5 eV in Figure 7b corresponds to an orbital generated as a result of the charge transfer interaction between the d-band and the σ_{C-H}^* orbital. The orbital with the energy of about -15 eV in Figure 7b corresponds an orbital generated as a result of the charge transfer interaction between the σ_{C-H} orbital and the d-band. The counterpart in the unoccupied region of this orbital is discussed in detail in the SI (see Figure S4). The lowering of the Fermi level would be unfavorable for C-H bond activation in terms of less effective charge transfer from the d-band to the σ_{C-H}^* orbital, but favorable in terms of more effective charge transfer from the σ_{C-H} orbital to the d-band. The converse is also true. The absence of linear correlation in the scatterplot shown in Figure S7a is likely to be a result of these two opposing effects.
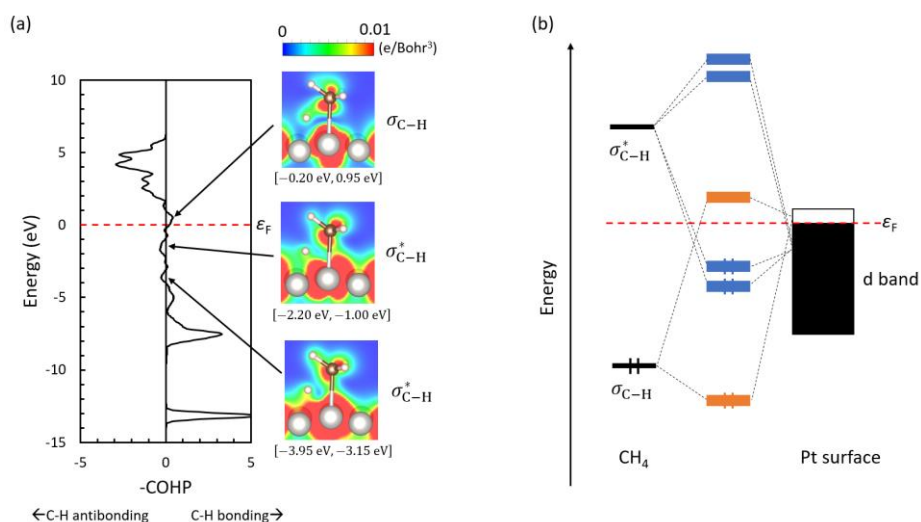
Figure 15. (a) COHP plot at the DFT level for the C-H bond that is about to be broken in the transition state structure shown in Figure 3a. Contour maps of the partial charge densities corresponding to the COHP peaks indicated by the arrows are also shown. The energy window of integration is shown below each map. (b) Orbital interaction diagram between the d-band of the Pt surface and the orbitals of methane estimated from the COHP spectrum shown in (a). Orbitals involved in the charge transfer from Pt to methane are shown in blue, and those involved in the charge transfer from CH_4 to Pt are shown in orange.

Returning to Figure 13, one can see that the CH_3 coupling is a reaction that is as difficult to occur on the Pt surface as the H-H coupling. However, Figure 4 shows that the activation barrier for the C-C coupling is more than twice as large as that for the H-H coupling. Furthermore, from Figure 13, one can see that the $\sigma^*_{Pt-Pt} + \pi^*_{C-C}$ orbital begins to rise from the higher energy position than the $\sigma^*_{Pt-Pt} + \sigma^*_{H-H}$ orbital does. This is a factor that prevents us from being convinced about the relationship between the activation energies of the C-C and H-H couplings. In the following, we shall analyze this.

Figure 12 shows that the destabilization of the system due to the rise of the σ^*_{H-H} orbital is, to some extent, compensated by the fall of the σ_{H-H} orbital. Similarly, Figure 13 shows that the fall of the σ_{C-C} orbital may compensate destabilization due to the rise of the σ^*_{C-C} orbital. However, it should be pointed out that one major difference between Figures 12 and 13 is that the degree of stabilization of the σ_{C-C} orbital is not as large as that of the σ_{H-H} orbital: from Figure 12b, the stabilization of the σ_{H-H} orbital reads about 2.4 eV, while that of the σ_{C-C} orbital reads about 1.1 eV from Figure 13b.

Figure 4 provides information to estimate how far the H-H and C-C bonds are away from the Pt surface; by and large, the C-C bond is located farther from the surface than the H-H bond. This means that the σ_{C-C} orbital does not interact with the surface as strongly as the σ_{H-H} orbital, and stabilization by the surface is smaller for the σ_{C-C} orbital. This would be one plausible explanation.

Figure 8 shows that there is essentially a difference between the two, even when they are not interacting with the surface. From Figure 8a, the degree of stabilization of the σ_{H-H} orbital can be read to be about 3.7 eV, while from Figure 8b, that of the σ_{C-C} orbital is about 2.6 eV. In addition to the fact that the C-C bond of ethane is less stabilized by the surface due to the steric hindrance of the C-H bonds, the fact

that the stabilization of the C-C bond is inherently less than that of the H-H bond may be responsible for the difficulty of the coupling of CH_3 species on the Pt surface.

Indeed, the bond dissociation energy of the C-C bond of ethane is 352 kJ/mol,[95] whereas that of the H-H bond is 436 kJ/mol,[96] so the above observation would make sense. However, we would like to know its cause, tracing it back to the MOs. Let us again inspect the Walsh diagram for ethane. Figure 16 shows how the MO energies of ethane change as the C-C bond shortens. The $1a_{1g}$ and e_u orbitals, which have a C-C bonding character, go down, while the $1a_{2u}$, e_g, and $2a_{2u}$ orbitals, which have a C-C antibonding character, go up. The behavior of the $2a_{1g}$ orbital, the HOMO, is very interesting. This orbital has a C-C bonding character, so it should continue to fall. However, as the C-C bond length approaches 1.5 Å, the decrease in energy becomes smaller and eventually the slope of the curve approaches zero. This behavior is not seen for the other bonding orbitals ($1a_{1g}$ and e_u), not seen in the HOMO of H_2 either. In a gedanken experiment where the C-C bond length gets even shorter than 1.5 Å, the energy of the $2a_{1g}$ orbital increases as the bond length decreases (see Figure S8). It is worth noting that this orbital has the same symmetry as the lowest energy orbital. Thus, they can interact with each other via a second-order energy process,[59] where nondegenerate orbital mixing plays an important role. The $1a_{1g}$ orbital is stabilized by the $2a_{1g}$, whereas the $2a_{1g}$ is destabilized by the $1a_{1g}$. Likewise, the $1a_{2u}$ and $2a_{2u}$ can interact with each other.
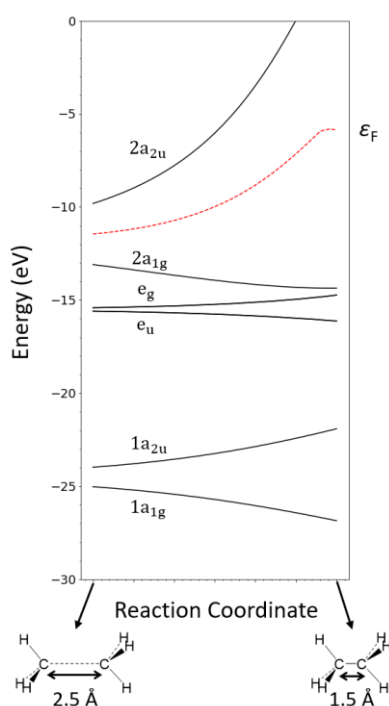

Figure 16. Walsh diagram at the eH level for the shortening of the C-C bond in ethane from 2.5 to 1.5 Å: the structural parameters other than the C-C bond length are not changed.

The mixing of the σ orbitals with the same symmetry is summarized in Figure 17. As a result of orbital mixing, the σ_s^+ and σ orbitals repel each other, resulting in the $1a_{1g}$ and $2a_{1g}$ orbitals depicted on the right side of the figure, respectively. The σ_s^+ orbital consists primarily of the 2s orbitals of the carbon

atoms, whereas the σ orbital consists primarily of the 2p orbitals of the carbon atoms. Thus, the interaction between them is termed s-p mixing. The same thing would happen for the σ_s^- and σ^* orbitals. However, the degree of repelling would be smaller because the energy difference between the σ_s^- and σ^* orbitals is greater than that between the σ_s^+ and σ. Note that the s-p mixing reduces the bonding character between the C atoms in the HOMO ($2a_{1g}$), making this orbital rather nonbonding. This reduces the degree of orbital overlap increase associated with the shortening of the C-C bond, so that orbital stabilization is not expected to be significant. Of course, the s-p mixing does not occur in the H_2 molecule, so the stabilization of the σ orbital in the H_2 molecule is greater than that in the C_2H_6 molecule. As such, the HOMO energy of C_2H_6 decreases at a slower rate than that of H_2 as shown in Figure 8. This is why the formation of the H-H bond is easier than that of the C-C bond.
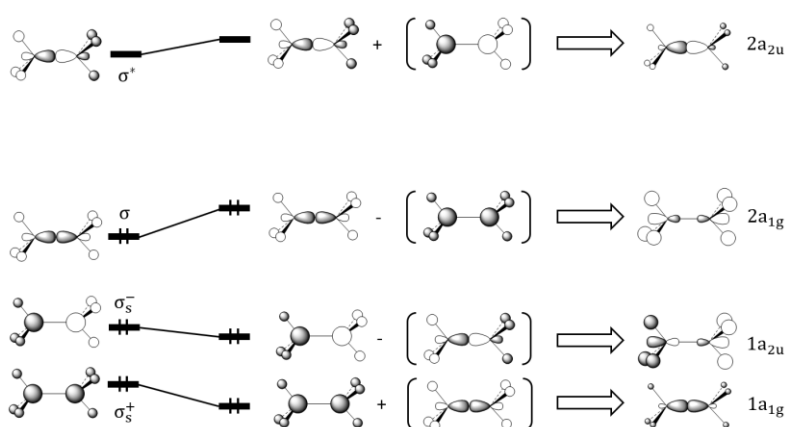

Figure 17. σ orbitals of ethane generated by considering the nondegenerate orbital mixing. For clarity, the π orbitals are omitted.

The activation barrier to C-C bond formation is greater than that to H-H bond formation because the HOMO of C_2H_6 is not stabilized as much as that of H_2 upon bond formation. As Figure 11 qualitatively shows, in the first place, the activation barrier to H-H bond formation itself is high, so the activation barrier to C-C bond formation is even higher. In situations where the activation barrier to H-H bond formation is lower, we would expect the activation barrier to C-C bond formation to also be reasonably low.

Trinquier et al.[85] studied the reductive elimination of H_2 from the dinuclear complex of $Mn_2H_{10}^{10-}$ using orbital correlation diagrams and found that this reaction is forbidden in the ground state. On the other hand, Tatsumi et al.[42] similarly studied the reductive elimination of R_2 from the mononuclear complex of *cis* d^8 L_2MR_2 to d^{10} L_2M, and found that this reaction is an allowed reaction. This difference corresponds well to the fact that reductive elimination from mononuclear complexes is well known, while that from dinuclear complexes is less so.[85] As the cluster model in Figure 10 shows, the surface reaction we show here is, in the language of organometallic chemistry, reductive elimination from the dinuclear center. If we could realize that from a mononuclear center on the surface, we would expect the activation barrier for that reaction to be lower. We have investigated two possibilities for achieving this.

One possibility is a coupling reaction at stepped surfaces. The highly stepped Pt surface of (332),

which contains a high density of edge sites, have been investigated experimentally as a good model system for nanoparticle catalysts.[97] Moreover, this surface has the second lowest surface energy after the (111) surface according to the Materials Project database.[98] At a step edge of this surface, a reaction similar to the C-C coupling on mononuclear complexes could be achieved. The energy diagram calculated for the coupling reaction of two CH_3 species at the step edge of the Pt(332) surface is shown in Figure 18a. Compared to the activation energy of the reaction shown in Figure 4b, that of this reaction is very low. This result supports the idea that coupling reactions are more likely to occur at mononuclear sites.
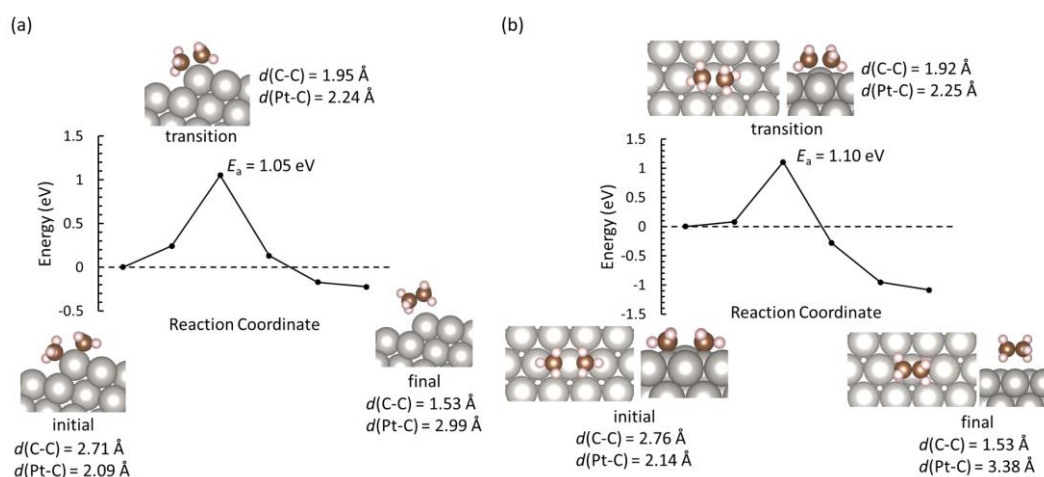

Figure 18. Energy profiles for the coupling reaction of two CH_3 species at (a) a step edge site in Pt(332) and (b) a mononuclear center in Pt(111) calculated at the DFT level. In each structure, the nearest neighbor C-C and Pt-C interatomic distances are indicated below.

Even on the (111) surface, a coupling reaction at a mononuclear center can be considered. This is the other possibility. As shown in Figure 18b, consider C-C coupling on a Pt atom flanked by two bridge sites at which CH_3 species are adsorbed. The activation energy for the C-C coupling reaction at this site is almost as low as at the step edge site shown in Figure 18a. These results convince us of the ease of C-C coupling at mononuclear centers. However, the CH_3 species adsorbed on the bridge sites are very close to each other, and a repulsive interaction would be present. On top of that, the most stable adsorption site for CH_3 on the Pt(111) surface is the on top site, not the bridge site.[41,99] For these reasons, it should be noted that a reasonable energy cost is required to bring the separated CH_3 species closer together to form the initial state in Figure 18b (see Figure S9). Thus, it would still be difficult to generate ethane on the Pt(111) surface from two CH_3 species although the discussion here is important in showing the role of the single Pt site.

Comparing Figure 4b with Figure 18b, one can see that the activation energy of the C-C coupling is dramatically reduced by moving from a dinuclear center to a mononuclear one. The complete energy profile of C-C coupling, including CH_3 diffusion on the Pt(111) surface, is shown in Figure S9. It can be seen that the reaction at the mononuclear site is preferred over the dinuclear site. In the following, we address a qualitative understanding of the difference based on the orbitals. The reaction shown in Figure 4b was analyzed using the Walsh diagram shown in Figure 13. A similar analysis was applied to the reaction shown

in Figure 18b, yielding the Walsh diagram shown in Figure 19. This Walsh diagram is essentially equivalent to the one in Figure 13: there is a level that rises from around -14 eV, which eventually correlates to the σ^*_{C-C} orbital; in the latter half of the reaction, the σ_{C-C} orbital appears to stabilize. This orbital seems to interact with the d_{z2} orbital of the Pt atom in a bonding manner. However, the two Walsh diagrams are not without differences. The most significant difference we would like to point out is that in Figure 19b, there is no level between -13.3 eV and the Fermi level, while in Figure 13b, some levels can be seen in that region. It is clear from Figures 13a and 19a that there are actually many levels in that region; in Figure 19b, any level whose energy is changing is not found in that region. Note that the orbital gradient threshold for selecting which orbitals to display is set to the same value in both figures. In the following, we illustrate what is brought about by this difference with a schematic representation of the orbital interaction.
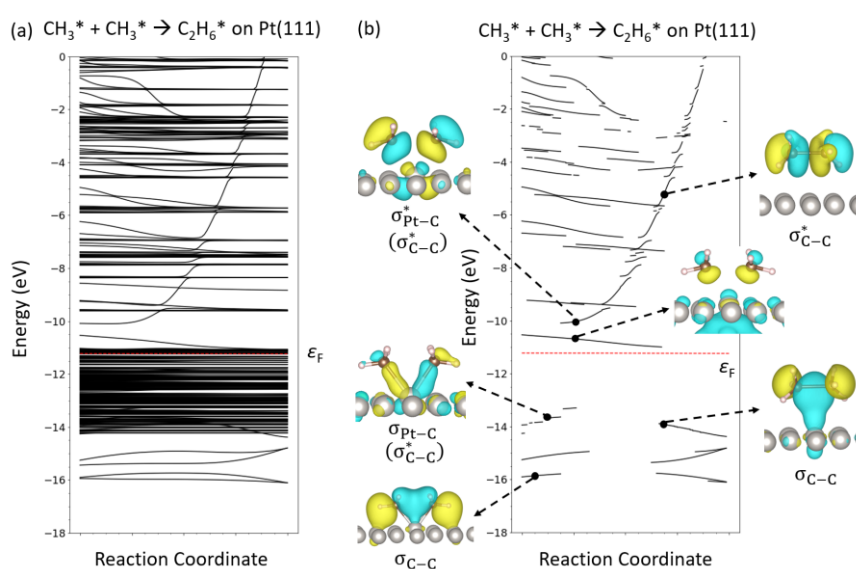

Figure 19. (a) eH-calculated evolution of the crystal orbital levels calculated at the Γ point along the reaction coordinate for $CH_3^* + CH_3^* \rightarrow C_2H_6^*$ at the mononuclear center in Pt(111). (b) Plots obtained by extracting the portion of the curves in (a) whose gradients are greater than 0.1 eV/Å. Selected Γ-point crystal orbital distributions are visualized with an isovalue of 0.03 bohr^{-3}.

Figures 20a and 20b show abstracted depiction of the essentially important avoided crossing patterns near the Fermi level in the Walsh diagrams shown in Figures 13 and 19, respectively. The situation shown in Figure 20a is a weakly avoided crossing, while the pattern illustrated by Figure 20b is indicative of a strongly avoided crossing. Whether a crossing is strongly avoided or weakly avoided can be determined whether the size of the gap at the avoided crossing point is large or small.[59] The upper orbital is caused by an antibonding interaction between the d orbital(s) of the Pt atom(s) and the p orbitals of the C atoms, whereas the lower orbital is caused by a bonding interaction between the d orbital(s) of the Pt atom(s) and the p orbitals of the C atoms. Thus, the size of the gap is determined by the overlap between the carbon and platinum orbitals. In the reaction at the mononuclear site, the orbital overlap is large even in the transition state, but that at the dinuclear site is small, which is due to the directivity of the Pt d_{z2} orbitals

and the C p_z orbitals. The strongly avoided crossing ensues in the reaction at the mononuclear site, while the weakly avoided crossing at the dinuclear site. Note that in Figure 20, the upper orbital is empty, but the lower is occupied. When a weakly avoided crossing occurs, the lower orbital must carry electrons closer to the Fermi level, which requires a larger energy cost. As such, the activation barrier is smaller for the coupling reaction at the mononuclear site.
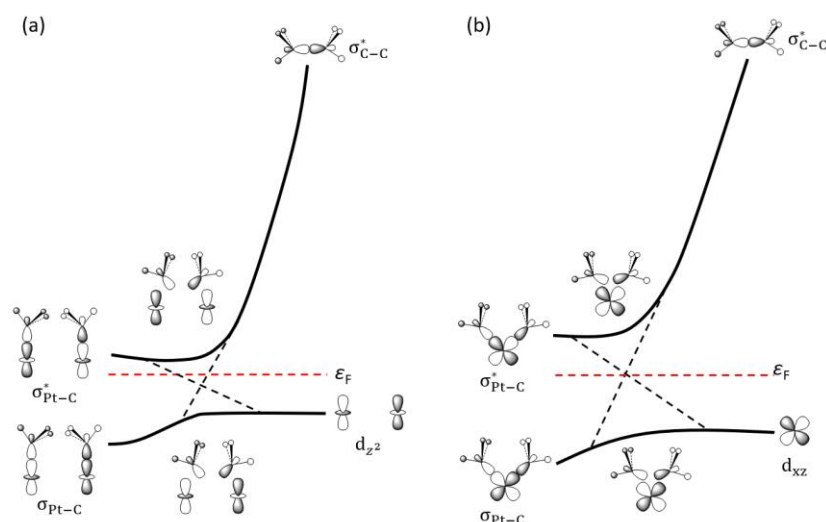

Figure 20. Schematic descriptions of essential avoided-crossing patterns abstracted from the Walsh diagrams for the C-C coupling reactions at the (a) dinuclear and (b) mononuclear sites shown in Figures 13 and 19, respectively.

3.5. How Can We Prevent Over-Oxidation of Methane?

Up to this point, on surfaces with low Fermi levels or at mononuclear sites, the activation barrier for the C-C coupling reaction has been found to become low. Nevertheless, the activation barrier for further dehydrogenation of CH_3^* to CH_2^* is much lower (see Figure 3b). Therefore, the over-oxidation takes precedence over the C-C coupling. In the following, we shall examine measures to reverse this relationship, and to do so, we must first of all contemplate why dehydrogenation of CH_3^* occurs easily.

Figure 21 shows the Walsh diagram calculated for the process of dehydrogenation of CH_3^* to CH_2^*. One will recognize the similarity to the Walsh diagram shown in Figure 7. Note that the activation energies for the $CH_4^* \rightarrow CH_3^* + H^*$ and $CH_3^* \rightarrow CH_2^* + H^*$ reactions are nearly equal. At the beginning of the reaction, the σ_{C-H}^* orbital goes down while the σ_{C-H} orbital goes up. Since the σ_{C-H} orbital is occupied, destabilization of this orbital is the main origin of the activation barrier. Although this orbital is destabilized, the 1s orbital of the dissociating hydrogen atom effectively overlaps with the d_{z^2} orbitals of the surrounding Pt atoms and is stabilized by a bonding interaction. Such an interaction has also been observed in $CH_4^* \rightarrow CH_3^* + H^*$ (see Figure 7). The presence of such a common interaction is a hindrance to designing methods to inhibit only one of the reactions.
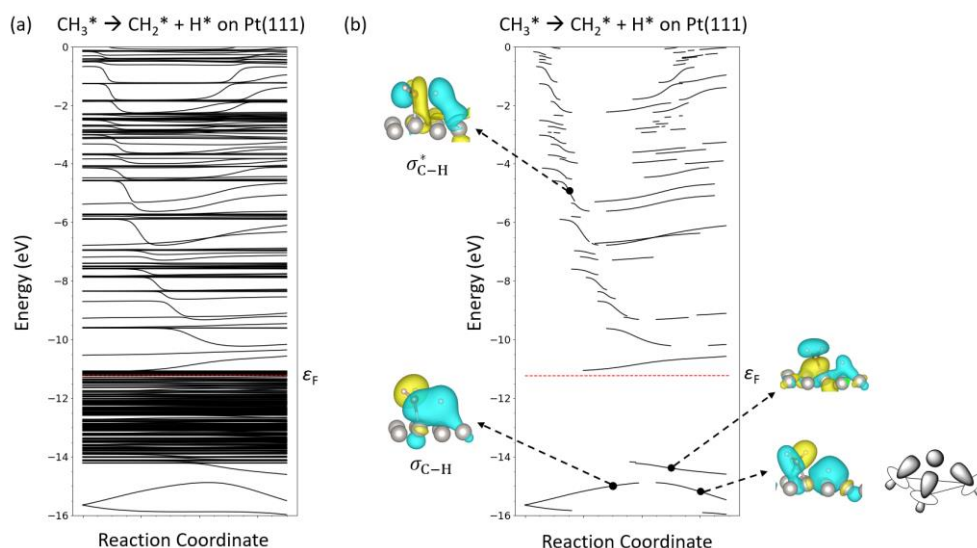
Figure 21. (a) eH-calculated evolution of the crystal orbital levels calculated at the Γ point along the reaction coordinate for the second C–H bond cleavage reaction of methane on the Pt surface. (b) Plots obtained by extracting the portion of the curves in (a) whose gradients are greater than 0.1 eV/Å. Selected Γ-point crystal orbital distributions are visualized with an isovalue of 0.03 bohr^{-3}. A schematic illustration of the bonding interaction between the d_{z^2} orbitals of platinum atoms and the 1s orbital of hydrogen is shown as an inset.

Let us turn to the orbital derived from σ_{C-H}^*. Therein lies a difference. The energy levels corresponding to the crystal orbitals generated by the in-phase combination of the σ_{C-H}^* orbital that has descended below the Fermi level and the Pt surface orbitals are seen in the energy ranges from -13.5 to -12.6 eV in Figure 7b and from -14.6 to -14.2 eV in Figure 21b. The crystal orbitals in question are reproduced in Figure 22. It can be seen that the d_{z^2} orbital of the Pt atom(s) interacts with the p_z orbital of the C atom. CH$_3$ is stabilized by one Pt atom, while CH$_2$ is stabilized by two. This is a reasonable result considering the valency of the carbon atom. We can also easily infer from the final state structure in Figure 3c that CH is stabilized by three Pt atoms. Thus, it is suggested from the orbital point of view that ensembles such as Pt-Pt duo and Pt-Pt-Pt trio contribute to the stabilization of the overoxidized states of methane. Such a critical influence of local topology of atomic connectivity on the catalyst surface on catalytic activity and selectivity is known as the ensemble effect. It is known that such ensemble effects are the main cause of coking on active catalytic metal surfaces such as Pt and Pd.[100,101] In recent years, attention has focused on alloys, especially single atom alloys (SAAs),[102,103,104] to prevent the presence of such ensembles.
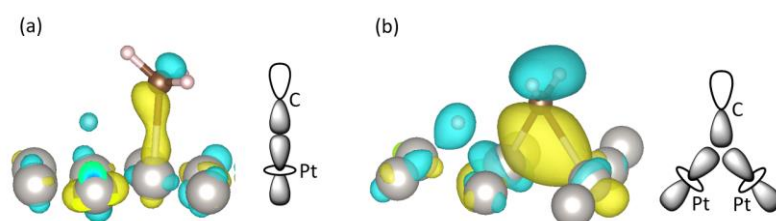

Figure 22. Stabilization of the σ_{C-H}^* orbital by a bonding interaction with the Pt surface orbitals in (a) CH$_4$*

→ CH₃* + H* and (b) CH₃* → CH₂* + H*. These orbitals were calculated at the eH level. An isovalue of 0.03 bohr^{-3} is used. A conceptual diagram for the orbital interaction is also shown on the right.

3.6. Rational Design of SAA Catalyst for NOCM

The present paper concludes with a study of NOCM on an SAA that produces neither Pt-Pt diatomic nor Pt-Pt-Pt triatomic ensemble. We consider an SAA containing Pt monatomic sites as active sites. The choice of the host is an important task. As presented in previous studies, inert elements such as Au, Ag, and Cu facilitate hydrogen desorption as well as are resistant to coking.[101,103] Therefore, it would be a good idea to choose a host element from among these metals. Henkelman and co-workers thoroughly evaluated the stability of various SAAs with these metals as a host by calculating the segregation energy.[103] They found that Pt₁/Ag(111) is not stable, while Pt₁/Au(111) and Pt₁/Cu(111) are stable. Indeed, synthesis and catalytic activity of both of them have been reported.[36,105] Methane activation by Cu-based SAAs has also been thoroughly investigated by Toyao et al. using a combination of DFT calculations and machine learning.[32]

The Pt₁/Au(111) and Pt₁/Cu(111) SAAs were respectively modeled by replacing one atom in the topmost layer of the close-packed Au(111)-(4 × 4) and Cu(111)-(4 × 4) slab models consisting of four atomic layers with a Pt atom. The bulk layer remains unalloyed. The Bader charges[106] calculated for the doped Pt atoms show that the magnitude of the negative charge of the Pt atom in the Au(111) surface is smaller than that in the Cu(111) surface (see Figure 23). This may be due to the fact that gold has a greater electronegativity than copper.[107] We have learned from Figure 14 and others that a cationic surface is more favorable for reductive elimination of ethane. As such, in the following, we shall consider Pt₁/Au(111), which has a smaller negative charge. The Au(111) surface without doping is also considered for comparison.

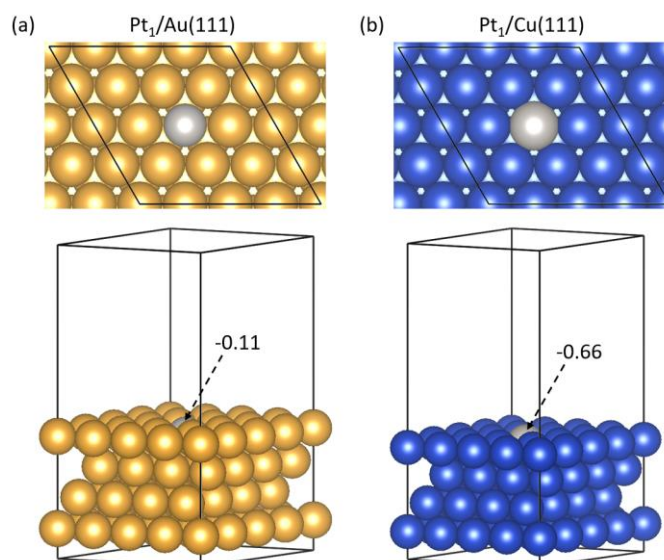**Figure 23.** Slab model structures for the (a) Pt₁/Au(111) and (b) Pt₁/Cu(111) SAAs. Top and oblique views are shown. The Bader charge calculated at the DFT level for the doped Pt atom is indicated.

Let us start with the first C-H bond cleavage reaction of methane. From Figure 24, one can see

that the C-H bond is easily cleaved on Pt_1/Au(111), but it is difficult to achieve it on Au(111). When this SAA is tested, this reaction is expected to occur only at the Pt active site. Compared to Pt(111) shown in Figure 3a, the activity can be said to be slightly reduced on Pt_1/Au(111). The activation energy for recombination to form methane (reverse reaction of the reaction in Figure 24a) on Pt_1/Au(111) is 0.34 eV. However, as shown in Figure S10, H* diffuses quickly over the surface with a small barrier of 0.24 eV, suggesting that the diffusion is preferred over the recombination. This suggests the possibility of hydrogen spillover.[108] CH_3* left on the active site is attracted to the Pt atom, but the activation barrier required for it to diffuse onto a neighboring Au atom does not exceed 1 eV as shown in Figure S11. Thus, C-H bond breaking and the diffusion of H* and CH_3* on Pt_1/Au(111) can reasonably occur.
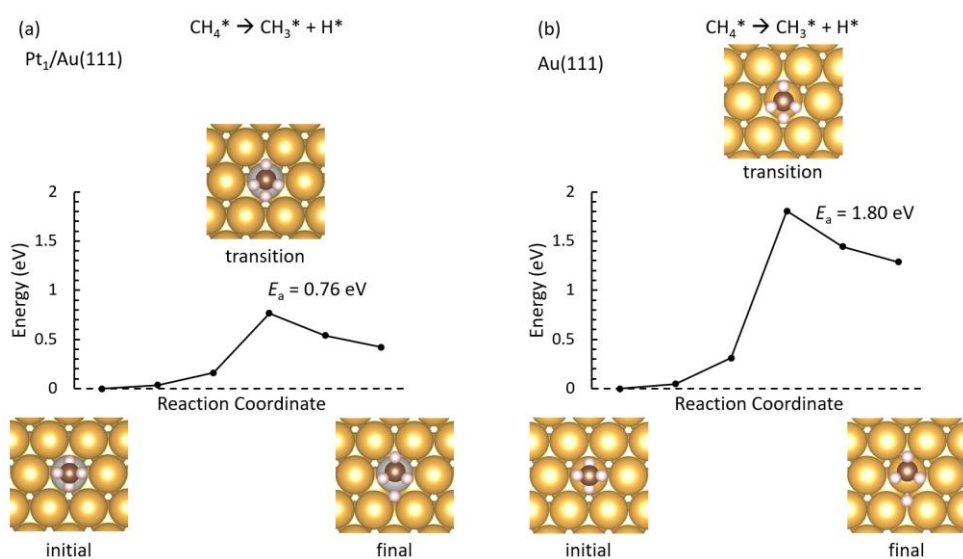

Figure 24. Energy profiles for CH_4* $\rightarrow$ CH_3* + H* on (a) Pt_1/Au(111) and (b) Au(111) calculated at the DFT level.

The difference in activation energy between Figures 24a and 24b is an issue worth pursuing. Let us see the Walsh diagram calculated for the C-H bond breaking on Pt_1/Au(111). Looking at Figure 25a, there is a region between -16.4 and -14 eV where a large number of energy levels are densely packed. They form the d-band of Au. It lies deeper than the Fermi level. On the other hand, that of Pt is in the region from -14.2 to -11 eV (see, for example, Figure 7a), and the Fermi level crosses it. In Figure 25b, one can see that the σ^*_{C-H} orbital rapidly descends with the progress of the reaction and further stabilizes below the Fermi level. From the crystal orbital distributions depicted in the figure, it appears that the σ^*_{C-H} orbital does not interact with surface orbitals in the early stage of the reaction, but interact with the Pt atom in the surface exclusively in the late stage of the reaction, resulting in π-bonding. There are two things to note in this Walsh diagram: 1) the surrounding Au atoms are not involved in the interaction with the σ^*_{C-H} orbital; 2) there are few occupied orbitals that are destabilized as the reaction proceeds.
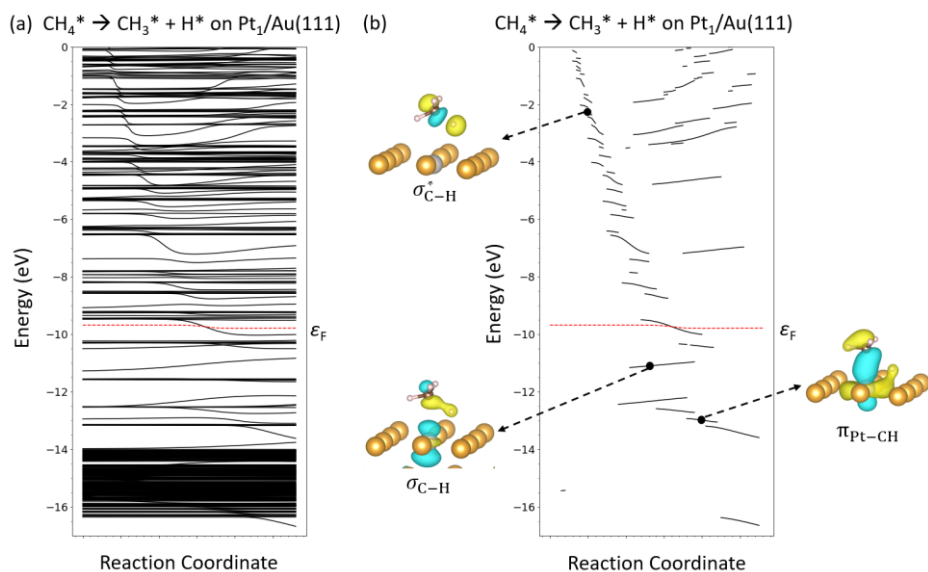
Figure 25. (a) eH-calculated evolution of the crystal orbital levels calculated at the Γ point along the reaction coordinate for the first C–H bond cleavage reaction of methane on Pt$_1$/Au(111). (b) Plots obtained by extracting the portion of the curves in (a) whose gradients are greater than 0.2 eV/Å. Selected Γ-point crystal orbital distributions are visualized with an isovalue of 0.03 bohr^{-3}.

Figure 26 shows a Walsh diagram for the C-H bond cleavage on Au(111). One can clearly see the energy increase of the σ_{C-H} orbital as the reaction proceeds. The amplitude of the wave function on the Au atoms just below the σ_{C-H} orbital is not large. This means that the interaction between the σ_{C-H} and the Au surface is small. This is probably what makes the difference. Since this feature leads to destabilization of the system, it makes sense that the activation barrier for the C-H bond cleavage on Au(111) is higher than that on Pt$_1$/Au(111).

Pt$_1$/Au(111) SAA has been shown to be a good catalyst candidate for NOCM. The key to its catalytic activity is to isolate Pt atoms and prevent the formation of Pt-Pt duo and Pt-Pt-Pt trio. Even if the bulk layer of the catalyst is also alloyed, it will still serve as a good catalyst for NOCM, as long as this condition is met (details are discussed in section 12 in the SI).
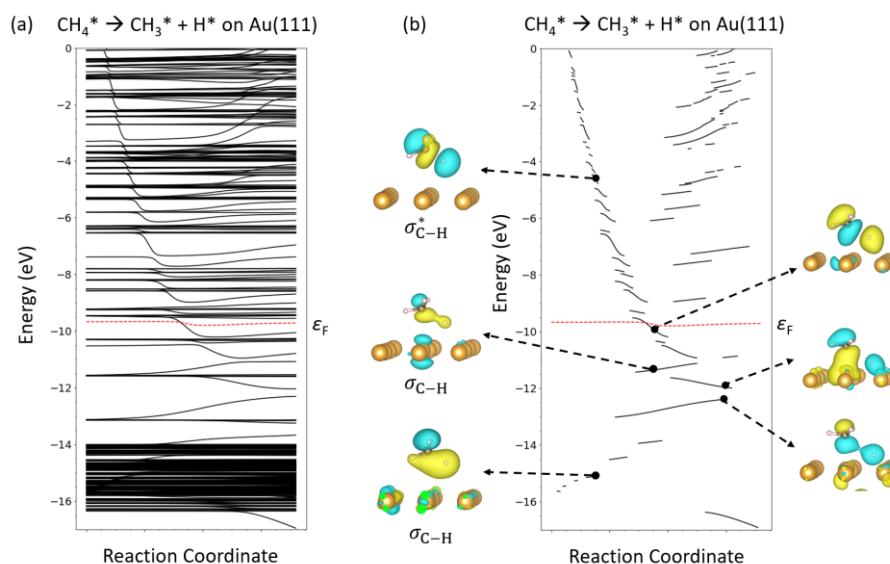
Figure 26. (a) eH-calculated evolution of the crystal orbital levels calculated at the Γ point along the reaction coordinate for the first C–H bond cleavage reaction of methane on Au(111). (b) Plots obtained by extracting the portion of the curves in (a) whose gradients are greater than 0.2 eV/Å. Selected Γ-point crystal orbital distributions are visualized with an isovalue of 0.03 bohr^{-3}.

In Figures 25 and 26, right at the middle of the reaction coordinate, one can see a σ_{C-H} orbital with an energy of about -11 eV. The interaction between this orbital and the surface orbital is antibonding. However, the σ_{C-H} orbital in Figure 7 interacts with the surface orbital in a bonding manner. On the Au surface, the σ_{C-H} orbital is destabilized, whereas on the Pt surface, the σ_{C-H} orbital is stabilized. As the reaction proceeds, the C-H bond is stretched, so the energy of the σ_{C-H} orbital generally rises. However, on the Pt surface, the destabilizing σ_{C-H} orbital is stabilized by the surface effectively.

Schematic diagrams to understand how the σ_{C-H} orbital interacts with the Pt and Au surfaces are shown in Figure 27. These figures are qualitative, based on Figures 7 and 26. What is important is that Pt has a higher d-band but lower Fermi level, while Au has a lower d-band but higher Fermi level. Note that the work function of Pt(111) is 5.9 eV, while that of Au(111) is 5.3 eV.[109,110] On the Pt surface, only the orbital produced by the bonding interaction of the σ_{C-H} with the d-band has an energy below the Fermi level. On the other hand, on the Au surface, both orbitals generated by the bonding and antibonding interactions of the σ_{C-H} with the d-band have energies below the Fermi level. Note that both of them contribute to the destabilization of the system upon the C-H bond elongation. This is probably the reason why the C-H bond is difficult to break on the Au surface.
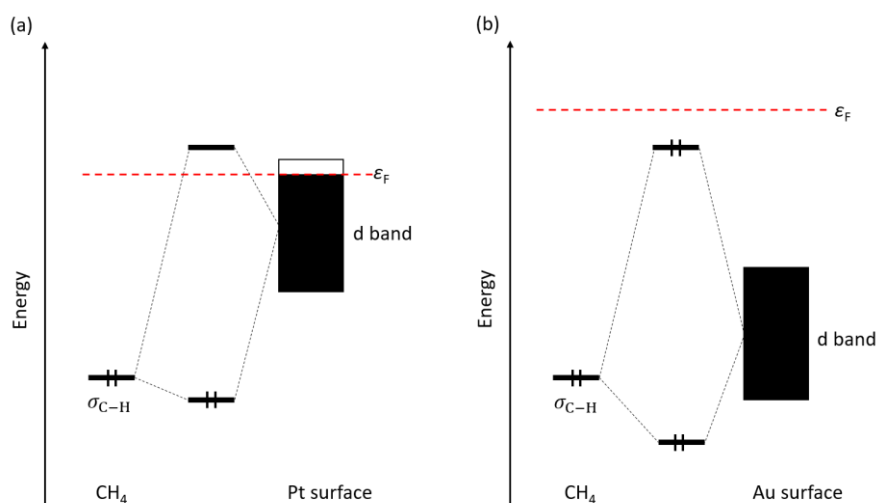
Figure 27. Schematic diagrams of the interaction between the d-band and σ_{C-H} orbital of methane on (a) Pt(111) and (b) Au(111). The d-band is represented by a rectangle. The shaded and unshaded areas represent the occupied and empty bands, respectively. The interaction between the σ_{C-H}^* and surface orbitals is omitted here.

There are still many issues to be considered, including the formation of a C-C bond, the formation of an H-H bond, and the control of over-oxidation. It may not be profitable to discuss Au(111) any further. From this point on, we shall concentrate on $Pt_1/Au(111)$. Figure 28 shows the coupling of two CH_3 species on $Pt_1/Au(111)$. The activation energy for C-C bond formation at a mononuclear site on the Pt surface is 1.10 eV, which has been further reduced to 0.86 eV at the Pt site in $Pt_1/Au(111)$. This suggests the importance of mononuclear sites in reductive elimination. A further interesting point in Figure 28 is that the energy of the intermediate is almost the same as that of the initial state. To produce a similar structure on the Pt surface, a high activation energy of 1.2 eV has to be overcome (see Figure S9). This difference is thought to be due to the difference in binding energy between the Pt-C and Au-C bonds.
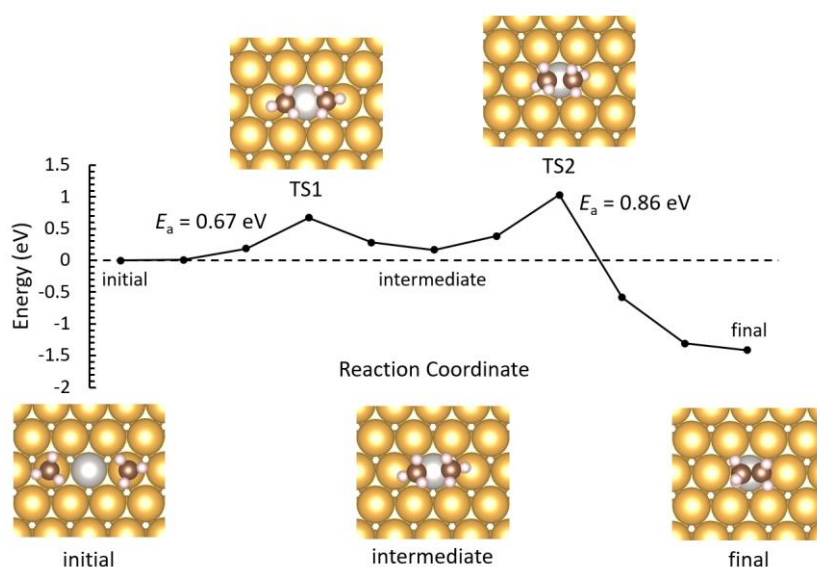

Figure 28. Energy profile for $CH_3^* + CH_3^* \rightarrow C_2H_6^*$ on $Pt_1/Au(111)$ calculated at the DFT level. This figure was

obtained by piecing together the results of two NEB calculations.

The binding energy (E_b) of the two CH_3 species to the surface can be evaluated by performing a single-point calculation with the CH_3 species pulled away from the surface and calculating the difference between that energy and the energy of the CH_3 species adsorbed on the surface. The results of the binding energy calculations are summarized in Figure 29. The CH_3 binding energy to the Au atom is small, while that to the Pt atom is large. Therefore, when the CH_3's on Pt_1/Au(111) approach the active Pt site, the binding energy becomes large because C-Pt bonds are formed. It is impossible to understand everything by relying only on the binding energy. However, it is possible to understand trends based on it. If one only looks at the binding energy, one may forget the repulsive energy of the CH_3's coming close to each other. On Pt_1/Au(111), the stabilization of the system due to the formation of the Pt-C bonds is offset by the destabilization due to the proximity of the CH_3's to each other, resulting in an almost thermoneutral reaction profile, as seen in the first half of the energy diagram in Figure 28. On the Pt surface, there is not much change in the binding energy of the CH_3's, so only the repulsive interaction between them is conspicuous.
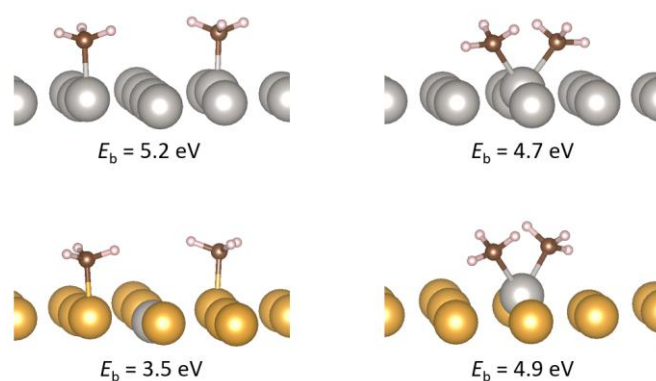

Figure 29. Binding energies (E_b) of two CH_3's to Pt(111) (top) and Pt_1/Au(111) (bottom) calculated for the cases where the CH_3's are far (left) and close to each other (right). These energies were calculated at the DFT level.

We shall then look at the energy diagrams for the important side reactions: the first is the H-H bond formation, which is essentially the same as the C-C bond formation. As shown in Figure 28, the activation energy for the reductive elimination of ethane from Pt_1/Au(111) is low, so the activation energy for that of H_2 from this surface should not be high. This is indeed true (see Figure 30a). The activation barrier required for two H atoms to come to the Pt active site is zero. The formation and desorption of H_2 requires an energy of 0.17 eV, which is not high. The next side reaction to be considered is the over-oxidation. In Figure 30b, the activation barrier for the further cleavage of the C-H bond of CH_3* is shown. The activation energy of 1.32 eV is the highest of all the processes we have seen on Pt_1/Au(111). Thus, with careful temperature control, Pt_1/Au(111) SAA may be used to selectively synthesize ethane from methane. Indeed, Sykes and co-workers[111,112] have observed that ethane is produced from iodomethane at temperatures as low as approximately 250 K using Ni_1/Au(111) and Pd_1/Au(111) SAAs.
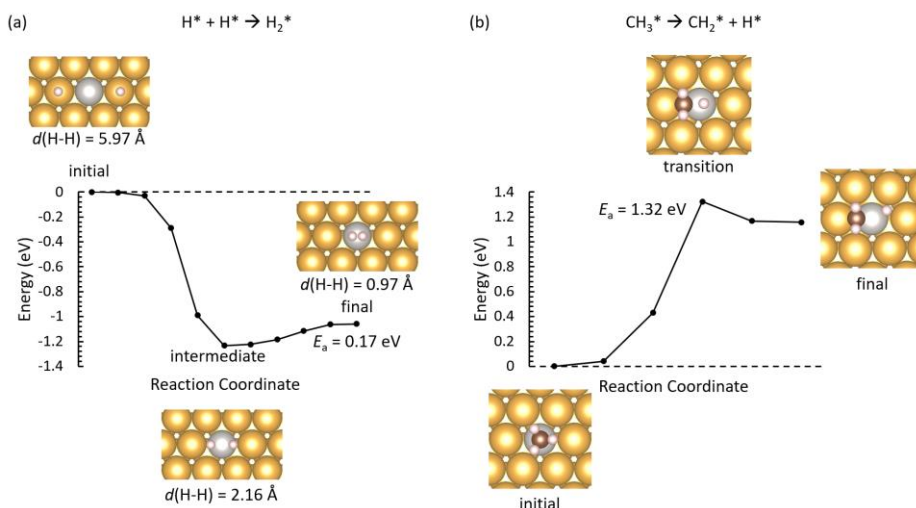
Figure 30. Energy profiles for (a) H* + H* $\rightarrow$ H$_2$* and (b) CH$_3$* $\rightarrow$ CH$_2$* + H* on Pt$_1$/Au(111) calculated at the DFT level. Energy diagram (a) was obtained by piecing together the results of two NEB calculations.

In closing, we shall confirm the characteristic that Pt$_1$/Au(111) SAA can inhibit over-oxidation from the point of view of crystal orbital evolution. A Walsh diagram for CH$_3$* $\rightarrow$ CH$_2$* + H* on this SAA is shown in Figure 31. This figure should be compared to Figure 21. As the reaction progresses, the σ^*_{C-H} orbital falls rapidly while the σ_{C-H} orbital rises gently. However, once the σ^*_{C-H} drops below the Fermi level, there is no clear indication that it is further stabilized. The distributions of the σ_{C-H} and σ^*_{C-H} show that the wave function of the C-H bond interacts well with that of Pt, but not so well with that of Au. From the above, it is safe to say that, as expected, moving from the Pt-Pt-Pt triangular ensemble to the Pt-Au-Au has helped to suppress over-oxidation. In relation to the graph in Figure 31b, lowering the threshold of the gradient of the energy level curves to be displayed does not generally change the conclusion (see Figure S12 for details).
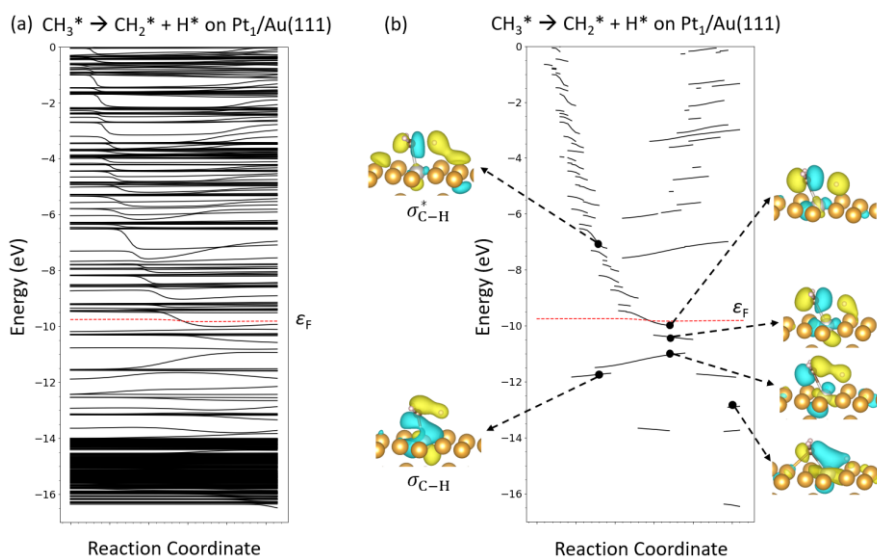

Figure 31. (a) eH-calculated evolution of the crystal orbital levels calculated at the Γ point along the reaction coordinate for CH$_3$* $\rightarrow$ CH$_2$* + H* on Pt$_1$/Au(111). (b) Plots obtained by extracting the portion of the curves in (a)

32

whose gradients are greater than 0.2 eV/Å. Selected Γ-point crystal orbital distributions are visualized with an isovalue of 0.03 bohr^{-3}.

4. Conclusions

NOCM is a process that produces ethane and hydrogen from two methane molecules. A competing process to this is the over-oxidation of methane. The processes of C-H bond cleavage and the formation of C-C and H-H bonds on catalyst surfaces are called oxidative addition and reductive elimination, respectively, in the language of organometallic chemistry. We have attempted to interpret such reactions on the surface of Pt in a molecular context by applying the Walsh diagram, or orbital correlation diagram, of molecular science to the bands, or crystal orbitals, of surface science.

In general, reductive elimination from dinuclear complexes is less likely to occur, but that from mononuclear complexes is more likely. Exactly the same is true for surface reactions. On the Pt surface, reductive elimination of two CH_3 species adsorbed on adjacent top sites requires a large amount of energy. However, that of two CH_3 species adsorbed on the same Pt atom occurs easily. In the case of reactions at a mononuclear center, the CH_3 species can strongly interact with surface orbitals in the transition state, whereas at a dinuclear center, the orbital overlap is smaller and so the interaction is weaker, making the transition state more unstable.

Pt has a high d-band and a low Fermi level compared to Au. This feature is very effective in stabilizing the C-H bond on Pt. Therefore, the C-H bond cleavage ability of the Pt surface is high compared to Au. In addition, an H atom resulting from the C-H bond cleavage is effectively stabilized by the Pt-Pt-Pt triangular ensemble on the surface.

Pt(111) is not desirable for controlling over-oxidation and promoting reductive elimination. Nevertheless, the first C-H bond of methane must be broken. To meet these conflicting requirements, we have proposed the SAA of Pt_1/Au(111) in which one Au atom in Au(111) is replaced by a Pt atom. The Pt dopant active site is reactive enough to cleave the first C-H bond of methane. However, the absence of the Pt-Pt-Pt ensemble prevents over-oxidation. On the other hand, the formation of mononuclear Pt sites is advantageous for the reductive elimination of ethane and hydrogen.

Author Information
Corresponding Author
*E-mail: tsuji.yuta.955@m.kyushu-u.ac.jp

ORCID
Yuta Tsuji: 0000-0003-4224-4532
Masataka Yoshida: 0000-0002-5621-955X
Takashi Kamachi: 0000-0001-9281-0454
Kazunari Yoshizawa: 0000-0002-6279-9722

Supporting Information: Extended Hückel parameters, Brillouin zone path, coupling of CH_3* and CH_2*, a Walsh diagram calculated at the DFT level, further analysis of the Walsh diagram shown in Figure 7, effects of unit cell charge on C-C coupling and C-H activation, further analysis for the Walsh diagram for ethane, complete energy profile of C-C coupling including CH_3 diffusion on Pt(111), diffusion of H and CH_3 on Pt_1/Au(111), further analysis of the Walsh diagram for $CH_3* \rightarrow CH_2* + H*$ on Pt_1/Au(111), effects of bulk layer alloying on catalytic activity, and atomic coordinates of optimized slab unit cells.

References

(1) Dai, Y.; Pavan Kumar, V.; Zhu, C.; MacLachlan, M. J.; Smith, K. J.; Wolf, M. O. Mesoporous Silica-Supported Nanostructured PdO/CeO_2 Catalysts for Low-Temperature Methane Oxidation. *ACS Appl. Mater. Interfaces* **2018**, *10*, 477-487.
(2) Karakaya, C.; Kee, R. J. Progress in the Direct Catalytic Conversion of Methane to Fuels and Chemicals. *Prog. Energy Combust. Sci.* **2016**, *55*, 60-97.
(3) Schüth, F. Making More from Methane. *Science* **2019**, *363*, 1282-1283.
(4) Tsuji, Y.; Kurino, K.; Yoshizawa, K. Mixed Anion Control of the Partial Oxidation of Methane to Methanol on the β-PtO_2 Surface. *ACS Omega* **2021**, *6*, 13858-13869.
(5) Xiao, Z.; Hou, F.; Zhang, J.; Zheng, Q.; Xu, J.; Pan, L.; Wang, L.; Zou, J.; Zhang, X.; Li, G. Methane Dry Reforming by Ni–Cu Nanoalloys Anchored on Periclase-Phase $MgAlO_x$ Nanosheets for Enhanced Syngas Production. *ACS Appl. Mater. Interfaces* **2021**, *13*, 48838-48854.
(6) Liang, T.-Y.; Senthil Raja, D.; Chin, K. C.; Huang, C.-L.; Sethupathi, S. A. P.; Leong, L. K.; Tsai, D.-H.; Lu, S.-Y. Bimetallic Metal-Organic Framework-Derived Hybrid Nanostructures as High-Performance Catalysts for Methane Dry Reforming. *ACS Appl. Mater. Interfaces* **2020**, *12*, 15183-15193.
(7) Postma, R. S.; Keijsper, D. J.; Morsink, B. F.; Siegers, E. H.; Mercimek, M. E. E.; Nieukoop, L. K.; van den Berg, H.; van der Ham, A. G. J.; Lefferts, L. Technoeconomic Evaluation of the Industrial Implementation of Catalytic Direct Nonoxidative Methane Coupling. *Ind. Eng. Chem. Res.* **2022**, *61*, 1, 566-579.
(8) Oh, S. C.; Schulman, E.; Zhang, J.; Fan, J.; Pan, Y.; Meng, J.; Liu, D. Direct Non-Oxidative Methane Conversion in a Millisecond Catalytic Wall Reactor. *Angew. Chem., Int. Ed.* **2019**, *58*, 7083-7086.

(9) Hayek, N. S.; Lucas, N. S.; Warwar Damouny, C.; Gazit, O. M. Critical Surface Parameters for the Oxidative Coupling of Methane over the Mn–Na–W/SiO$_2$ Catalyst. *ACS Appl. Mater. Interfaces* **2017**, *9*, 40404-40411.

(10) Xiao, Y.; Varma, A. Highly Selective Nonoxidative Coupling of Methane over Pt-Bi Bimetallic Catalysts. *ACS Catal.* **2018**, *8*, 2735-2740.

(11) Manion, J. A. Evaluated Enthalpies of Formation of the Stable Closed Shell C1 and C2 Chlorinated Hydrocarbons. *J. Phys. Chem. Ref. Data* **2002**, *31*, 123-172.

(12) Cox, J. D.; Wagman, D. D.; Medvedev, V. A. *CODATA Key Values for Thermodynamics*; Hemisphere Publishing Corp.: New York, 1984.

(13) Keller, G. E.; Bhasin, M. M. Synthesis of Ethylene via Oxidative Coupling of Methane: I. Determination of Active Catalysts. *J. Catal.* **1982**, *73*, 9-19.

(14) Arakawa, H.; Aresta, M.; Armor, J. N.; Barteau, M. A.; Beckman, E. J.; Bell, A. T.; Bercaw, J. E.; Creutz, C.; Dinjus, E.; Dixon, D. A.; Domen, K.; DuBois, D. L.; Eckert, J.; Fujita, E.; Gibson, D. H.; Goddard, W. A.; Goodman, D. W.; Keller, J.; Kubas, G. J.; Kung, H. H.; Lyons, J. E.; Manzer, L. E.; Marks, T. J.; Morokuma, K.; Nicholas, K. M.; Periana, R.; Que, L.; Rostrup-Nielson, J.; Sachtler, W. M. H.; Schmidt, L. D.; Sen, A.; Somorjai, G. A.; Stair, P. C.; Stults, B. R.; Tumas, W. Catalysis Research of Relevance to Carbon Management: Progress, Challenges, and Opportunities. *Chem. Rev.* **2001**, *101*, 953-996.

(15) Gao, Y.; Neal, L. M.; Ding, D.; Wu, W.; Baroi, C.; Gaffney, A.; Li, F. Recent Advances in Intensified Ethylene Production – A Review. *ACS Catal.* **2019**, *9*, 8592-5621.

(16) Nishimura, S.; Ohyama, J.; Kinoshita, T.; Dinh Le, S.; Takahashi, K. Revisiting Machine Learning Predictions for Oxidative Coupling of Methane (OCM) Based on Literature Data. *ChemCatChem* **2020**, *12*, 5888-5892.

(17) Zhang, T. Recent Advances in Heterogeneous Catalysis for the Nonoxidative Conversion of Methane. *Chem. Sci.* **2021**, *12*, 12529-12545.

(18) Levin, N.; Lengyel, J.; Eckhard, J. F.; Tschurl, M.; Heiz, U. Catalytic Non-Oxidative Coupling of Methane on Ta$_8$O$_2^+$. *J. Am. Chem. Soc.* **2020**, *142*, 5862-5869.

(19) Galadima, A.; Muraza, O. Revisiting the Oxidative Coupling of Methane to Ethylene in the Golden Period of Shale Gas: A Review. *J. Ind. Eng. Chem.* **2016**, *37*, 1-13.

(20) Arndt, S.; Laugel, G.; Levchenko, S.; Horn, R.; Baerns, M.; Scheffler, M. A Critical Assessment of Li/MgO-Based Catalysts for the Oxidative Coupling of Methane. *Catal. Rev.* **2011**, *53*, 424-514.

(21) Belgued, M.; Pareja, P.; Amariglio, A.; Amariglio, H. Conversion of Methane into Higher Hydrocarbons on Platinum. *Nature* **1991**, *352*, 789-790.

(22) Guo, X.; Fang, G.; Li, G.; Ma, H.; Fan, H.; Yu, L.; Ma, C.; Wu, X.; Deng, D.; Wei, M.; Tan, D.; Si, R.; Zhang, S.; Li, J.; Sun, L.; Tang, Z.; Pan, X.; Bao, X. Direct, Nonoxidative Conversion of Methane to Ethylene, Aromatics, and Hydrogen. *Science* **2014**, *344*, 616-619.

(23) Sakbodin, M.; Wu, Y.; Oh, S. C.; Wachsman, E. D.; Liu, D. Hydrogen-Permeable Tubular Membrane Reactor: Promoting Conversion and Product Selectivity for Non-Oxidative Activation of Methane over an FeVSiO$_2$ Catalyst. *Angew. Chem. Int. Ed.* **2016**, *55*, 16149-16152.

(24) Liu, L.; Das, S.; Zhang, Z.; Kawi, S. Nonoxidative Coupling of Methane over Ceria-Supported Single-Atom Pt Catalysts in DBD Plasma. *ACS Appl. Mater. Interfaces* **2022**, *14*, 5363-5375.

(25) Guéret, C.; Daroux, M.; Billaud, F. Methane Pyrolysis: Thermodynamics. *Chem. Eng. Sci.* **1997**, *52*, 815-827.

(26) Schwach, P.; Pan, X.; Bao, X. Direct Conversion of Methane to Value-Added Chemicals over Heterogeneous Catalysts: Challenges and Prospects. *Chem. Rev.* **2017**, *117*, 8497-8520.

(27) Spivey, J. J.; Hutchings, G. Catalytic Aromatization of Methane. *Chem. Soc. Rev.* **2014**, *43*, 792-803.

(28) Aziz, M. A. A.; Jalil, A. A.; Wongsakulphasatch, S.; Vo, D.-V. N. Understanding the Role of Surface Basic Sites of Catalysts in CO$_2$ Activation in Dry Reforming of Methane: A Short Review. *Catal. Sci. Technol.* **2020**, *10*, 35-45.

(29) Vollmer, I.; Yarulina, I.; Kapteijn, F.; Gascon, J. Progress in Developing a Structure-Activity Relationship for the Direct Aromatization of Methane. *ChemCatChem* **2019**, *11*, 39-52.

(30) Golinskii, D. V.; Vinichenko, N. V.; Zatolokina, E. V.; Pashkov, V. V.; Paukshtis, E. A.; Gulyaeva, T. I.; Pavlyuchenko, P. E.; Krol', O. V.; Belyi, A. S. Modern Catalysts and Methods of Nonoxidative Methane Conversion. *Russ. J. Gen. Chem.* **2020**, *90*, 1104–1119.

(31) Kamachi, T.; Saito, M.; Tsuji, Y.; Yoshizawa, K. Catalyst Informatics on Methane Activation on Carious Metal Alloys. *J. Comput. Chem. Jpn.* **2017**, *16*, 147-150.

(32) Toyao, T.; Suzuki, K.; Kikuchi, S.; Takakusagi, S.; Shimizu, K.; Takigawa, I. Toward Effective Utilization of Methane: Machine Learning Predic-Tion of Adsorption Energies on Metal Alloys. *J. Phys. Chem. C* **2018**, *122*, 8315-8326.

(33) Hori, M.; Tsuji, Y.; Yoshizawa, K. Bonding of C_1 Fragments on Metal Nanoclusters: A Search for Methane Conversion Catalysts with Swarm Intelligence. *Phys. Chem. Chem. Phys.* **2021**, *23*, 14004-14015.

(34) Yoshida, M.; Tsuji, Y.; Iguchi, S.; Nishiguchi, H.; Yamanaka, I.; Abe, H.; Kamachi, T.; Yoshizawa, K. Toward Computational Screening of Bimetallic Alloys for Methane Activation: A Case Study of MgPt Alloy. *ACS Catal.* **2022**, *12*, 9458-9472.

(35) Gerceker, D.; Motagamwala, A. H.; Rivera-Dones, K. R.; Miller, J. B.; Huber, G. W.; Mavrikakis, M.; Dumesic, J. A. Methane Conversion to Ethylene and Aromatics on PtSn Catalysts. *ACS Catal.* **2017**, *7*, 2088-2100.

(36) Marcinkowski, M. D.; Darby, M. T.; Liu, J.; Wimble, J. M.; Lucci, F. R.; Lee, S.; Michaelides, A.; Flytzani-Stephanopoulos, M.; Stamatakis, M.; Sykes, E. C. H. Pt/Cu Single-Atom Alloys as Coke-Resistant Catalysts for Efficient C-H Activation. *Nat. Chem.* **2018**, *10*, 325-332.

(37) Nakaya, Y.; Hirayama, J.; Yamazoe, S.; Shimizu, K.; Furukawa, S. Single-Atom Pt in Intermetallics as an Ultrastable and Selective Catalyst for Propane Dehydrogenation. *Nat. Commun.* **2020**, *11*, 2838.

(38) Chen, Y.; Vlachos, D. G. Density Functional Theory Study of Methane Oxidation and Reforming on Pt(111) and Pt(211). *Ind. Eng. Chem. Res.* **2012**, *51*, 12244-12252.

(39) Viñes, F.; Lykhach, Y.; Staudt, T.; Lorenz, M. P. A.; Papp, C.; Steinrück, H.; Libuda, J.; Neyman, K. M.; Görling, A. Methane Activation by Platinum: Critical Role of Edge and Corner Sites of Metal Nanoparticles. *Chem.—Eur. J.* **2010**, *16*, 6530-6539.

(40) Oana, M.; Hoffmann, R.; Abruña, H. D.; DiSalvo, F. Adsorption of CO on $PtBi_2$ and PtBi Surfaces. *J. Surf. Sci.* **2005**, *574*, 1-16.

(41) Papoian, G.; Nørskov, J. K.; Hoffmann, R. A Comparative Theoretical Study of the Hydrogen, Methyl, and Ethyl Chemisorption on the Pt (111) Surface. *J. Am. Chem. Soc.* **2000**, *122*, 4129-4144.

(42) Tatsumi, K.; Hoffmann, R.; Yamamoto, A.; Stille, J. K. Reductive Elimination of d^8-Organotransition Metal Complexes. *Bull. Chem. Soc. Jpn.* **1981**, *54*, 1857-1867.

(43) Saillard, J. Y.; Hoffmann, R. Carbon-Hydrogen and Hydrogen-Hydrogen Activation in Transition Metal Complexes and on Surfaces. *J. Am. Chem. Soc.* **1984**, *106*, 2006-2026.

(44) Kresse, G.; Hafner, J. Ab Initio Molecular Dynamics for Liquid Metals. *Phys. Rev. B* **1993**, *47*, 558-561.

(45) Kresse, G.; Hafner, J. Ab Initio Molecular-Dynamics Simulation of the Liquid-Metal-Amorphous-Semiconductor Transition in Germanium. *Phys. Rev. B* **1994**, *49*, 14251-14269.

(46) Kresse, G.; Furthmüller, J. Efficiency of Ab-Initio Total Energy Calculations for Metals and Semiconductors Using a Plane-Wave Basis Set. *Comput. Mater. Sci.* **1996**, *6*, 15-50.

(47) Kresse, G.; Furthmüller, J. Efficient Iterative Schemes for Ab Initio Total-Energy Calculations Using a Plane-Wave Basis Set. *Phys. Rev. B* **1996**, *54*, 11169-11186.

(48) Perdew, J. P.; Burke, K.; Ernzerhof, M. Generalized Gradient Approximation Made Simple. *Phys. Rev. Lett.* **1996**, *77*, 3865-3868.

(49) Blöchl, P. E. Projector Augmented-Wave Method. *Phys. Rev. B* **1994**, *50*, 17953-17979.

(50) Kresse, G.; Joubert, D. From Ultrasoft Pseudopotentials to the Projector Augmented-Wave Method. *Phys. Rev. B* **1999**, *59*, 1758-1775.

(51) Grimme, S.; Ehrlich, S.; Goerigk, L. Effect of the Damping Function in Dispersion Corrected Density Functional Theory. *J. Comput. Chem.* **2011**, *32*, 1456-1465.

(52) Momma, K.; Izumi, F. VESTA 3 for Three-Dimensional Visualization of Crystal, Volumetric and Morphology Data. *J. Appl. Crystallogr.* **2011**, *44*, 1272-1276.

(53) Henkelman, G.; Uberuaga, B. P.; Jónsson, H. A Climbing Image Nudged Elastic Band Method for Finding Saddle Points and Minimum Energy Paths. *J. Chem. Phys.* **2000**, *113*, 9901-9904.

(54) Jónsson, H.; Mills, G.; Jacobsen, K. W. Nudged Elastic Band Method for Finding Minimum Energy Paths of Transitions. In *Classical and Quantum Dynamics in Condensed Phase Simulations*; Berne, B. J., Ciccotti, G., Coker, D. F., Eds.; World Scientific: Singapore, 1998; pp 385-404.

(55) Henkelman, G.; Jónsson, H. Improved Tangent Estimate in the Nudged Elastic Band Method for Finding Minimum Energy Paths and Saddle Points. *J. Chem. Phys.* **2000**, *113*, 9978-9985.

(56) The transition state tools implementation for VASP is available at http://theory.cm.utexas.edu/vtsttools/

(57) Woodward, R. B.; Hoffmann, R. The Conservation of Orbital Symmetry. *Angew. Chem., Int. Ed. Engl.* **1969**, *8*, 781-853.

(58) Hoffmann, R.; Woodward, R. B. Conservation of Orbital Symmetry. *Acc. Chem. Res.* **1968**, *1*, 17-22.

(59) Albright, T. A.; Burdett, J.; Whangbo, M.-H. *Orbital Interactions in Chemistry*, 2nd ed.; Wiley: Hoboken, 2013.

(60) Atkins, P. W. *Shriver & Atkins' Inorganic Chemistry*; Oxford University Press: Oxford, 2010.

(61) Tsuji, Y.; Yoshizawa, K. Mixed-Anion Control of C-H Bond Activation of Methane on the IrO_2 Surface. *J. Phys. Chem. C* **2020**, *124*, 17058-17072.

(62) Dronskowski, R.; Bloechl, P. E. Crystal Orbital Hamilton Populations (COHP): Energy-Resolved Visualization of Chemical Bonding in Solids Based on Density-Functional Calculations. *J. Phys. Chem.* **1993**, *97*, 8617-8624.

(63) Tsuji, Y.; Okazawa, K.; Kobayashi, Y.; Kageyama, H.; Yoshizawa, K. Electronic Origin of Catalytic Activity of TiH_2 for Ammonia Synthesis. *J. Phys. Chem. C* **2021**, *125*, 3948-3960.

(64) Smidstrup, S.; Pedersen, A.; Stokbro, K.; Jónsson, H. Improved Initial Guess for Minimum Energy Path Calculations. *J. Chem. Phys.* **2014**, *140*, 214106.

(65) Smidstrup, S.; Markussen, T.; Vancraeyveld, P.; Wellendorff, J.; Schneider, J.; Gunst, T.; Verstichel, B.; Stradi, D.; Khomyakov, P. A.; Vej-Hansen, U. G.QuantumATK: An Integrated Platform of Electronic and Atomic-Scale Modelling Tools. *J. Phys.: Condens. Matter* **2020**, *32*, 015901.

(66) Stokbro, K.; Petersen, D. E.; Smidstrup, S.; Blom, A.; Ipsen, M.; Kaasbjerg, K. Semiempirical Model for Nanoscale Device Simulations. *Phys. Rev. B* **2010**, *82*, 075420.

(67) Monkhorst, H. J.; Pack, J. D. Special Points for Brillouin-Zone Integrations. *Phys. Rev. B* **1976**, *13*, 5188-5192.

(68) Alvarez, S. *Table of Parameters for Extended Hückel Calculations*; Universitat de Barcelona: Barcelona, Spain, 1993.

(69) Ammeter, J. H.; Bürgi, H.-B.; Thibeault, J.; Hoffmann, R. Counterintuitive Mixing in Semiempirical and Ab Initio Molecular Orbital Calculations. *J. Am. Chem. Soc.* **1978**, *100*, 3686-3692.

(70) Tsuji, Y.; Saito, M.; Yoshizawa, K. Dynamics and Energetics of Methane on the Surfaces of Transition Metal Oxides. In *Direct Hydroxylation of Methane*; Yoshizawa, K., Ed.; Springer: Singapore, 2020; pp 101-133.

(71) Qi, Q.; Wang, X.; Chen, L.; Li, B. Methane Dissociation on Pt(1 1 1), Ir(1 1 1) and PtIr(1 1 1) surface: A Density Functional Theory Study. *Appl. Surf. Sci.* **2013**, *284*, 784-791.

(72) Hannagan, R. T.; Giannakakis, G.; Réocreux, R.; Schumann, J.; Finzel, J.; Wang, Y.; Michaelides, A.; Deshlahra, P.; Christopher, P.; Flytzani-Stephanopoulos, M.; Stamatakis, M.; Sykes, E. C. H. First-Principles Design of a Single-Atom-Alloy Propane Dehydrogenation Catalyst. *Science* **2021**, *372*, 1444-1447.

(73) Hoffmann, R. A Chemical and Theoretical Way to Look at Bonding on Surfaces. *Rev. Mod. Phys.* **1988**, *60*, 601-628.

(74) Hoffmann, R. *Solids and Surfaces: A Chemist's View of Bonding in Extended Structures*; Wiley-VCH: Weinheim, 1988.

(75) Zheng, C.; Apeloig, Y.; Hoffmann, R. Bonding and Coupling of C_1 Fragments on Metal Surfaces. *J. Am. Chem. Soc.* **1988**, *110*, 749-774.

(76) Hoffmann, R. Reductive Elimination. In *Frontiers of Chemistry*; Laidler, K. J., Ed.; Pergamon Press: Oxford, 1982.

(77) Speight, J. G. *Handbook of Gasification Technology: Science, Processes, and Applications*; John Wiley & Sons: Hoboken, 2020.

(78) Weller, M.; Overton, T.; Rourke, J.; Amstrong, F. *Inorganic Chemistry*, 6th ed.; Oxford University Press: Oxford, 2014.

(79) Davis, B. H. Fischer-Tropsch Synthesis: Reaction Mechanisms for Iron Catalysts. *Catal. Today* **2009**, *141*, 25-33.

(80) Liu, Q.; Hoffmann, R. The Bare and Acetylene Chemisorbed Si(001) Surface, and the Mechanism of Acetylene Chemisorption. *J. Am. Chem. Soc.* **1995**, *117*, 4082-4092.

(81) Pettifor, D. G. Individual Orbital Contributions to the SCF Virial in Homonuclear Diatomic Molecules. *J. Chem. Phys.* **1978**, *69*, 2930-2931.

(82) Averill, F. W.; Painter, G. S. Orbital Forces and Chemical Bonding in Density-Functional Theory: Application to First-Row Dimers. *Phys. Rev. B* **1986**, *34*, 2088-2096.

(83) Stuyver, T.; Chen, B.; Zeng, T.; Geerlings, P.; De Proft, F.; Hoffmann, R. Do Diradicals Behave Like Radicals? *Chem. Rev.* **2019**, *119*, 11291-11351.

(84) Nakatsuji, H.; Hada, M.; Yonezawa, T. Theoretical Study on the Chemisorption of a Hydrogen Molecule on Palladium. *J. Am. Chem. Soc.* **1987**, *109*, 1902-1912.

(85) Trinquier, G.; Hoffmann, R. Dinuclear Reductive Eliminations. *Organometallics* **1984**, *3*, 370-380.

(86) Hafner, J. Ab-Initio Simulations of Materials Using VASP: Density-Functional Theory and Beyond. *J. Comput. Chem.* **2008**, *29*, 2044-2078.

(87) Huang, G.-Y.; Wang, C.-Y.; Wang, J.-T. Detailed Check of the LDA+U and GGA+U Corrected Method for Defect Calculations in Wurtzite ZnO. *Comput. Phys. Commun.* **2012**, *183*, 1749-1752.

(88) Miao, M. S.; Hoffmann, R. High Pressure Electrides: A Predictive Chemical and Physical Theory. *Acc. Chem. Res.* **2014**, *47*, 1311-1317.

(89) Tsuji, Y.; Hoffmann, R.; Miller, J. S. Revisiting Ir(CO)$_3$Cl. *Polyhedron* **2016**, *103*, 141-149.

(90) Hammond, G. S. A Correlation of Reaction Rates. *J. Am. Chem. Soc.* **1955**, *77*, 334-338.

(91) Deringer, V. L.; Tchougréeff, A. L.; Dronskowski, R. Crystal Orbital Hamilton Population (COHP) Analysis as Projected from Plane-Wave Basis Sets. *J. Phys. Chem. A* **2011**, *115*, 5461-5466.

(92) Maintz, S.; Deringer, V. L.; Tchougréeff, A. L.; Dronskowski, R. Analytic Projection from Plane-Wave and PAW Wavefunctions and Application to Chemical-Bonding Analysis in Solids. *J. Comput. Chem.* **2013**, *34*, 2557-2567.

(93) Maintz, S.; Deringer, V. L.; Tchougréeff, A. L.; Dronskowski, R. LOBSTER: A Tool to Extract Chemical Bonding from Plane-Wave Based DFT. *J. Comput. Chem.* **2016**, *37*, 1030-1035.

(94) Rauk, A. *Orbital Interaction Theory of Organic Chemistry*, 2nd ed.; John Wiley & Sons: New York, 2001.

(95) Schobert, H. H. *The Chemistry of Hydrocarbon Fuels*; Butterworths: London, 1990.

(96) Osman, R.; Perutz, R. N.; Rooney, A. D.; Langley, A. J. Picosecond Photolysis of a Metal Dihydride: Rapid Reductive Elimination of Dihydrogen from Ru(dmpe)$_2$H$_2$ (dmpe = (CH$_3$)$_2$PCH$_2$CH$_2$P(CH$_3$)$_2$) *J. Phys. Chem.* **1994**, *98*, 3562-3563.

(97) Somorjai, G. A.; Beaumont, S. K.; Alayoglu, S. Determination of Molecular Surface Structure, Composition, and Dynamics under Reaction Conditions at High Pressures and at the Solid-Liquid Interface. *Angew. Chem., Int. Ed.* **2011**, *50*, 10116-10129.

(98) Tran, R.; Xu, Z.; Radhakrishnan, B.; Winston, D.; Sun, W.; Persson, K. A.; Ong, S. P. Surface Energies of Elemental Crystals. *Sci. Data* **2016**, *3*, 160080.

(99) Tsuji, Y.; Yoshizawa, K. Adsorption Site Preference Determined by Triangular Topology: Application of the Method of Moments to Transition Metal Surfaces. *J. Phys. Chem. C* **2022**, *126*, 13505-13519.

(100) Wegener, E. C.; Bukowski, B. C.; Yang, D.; Wu, Z.; Kropf, A. J.; Delgass, W. N.; Greeley, J.; Zhang, G.; Miller, J. T. Intermetallic Compounds as an Alternative to Single-Atom Alloy Catalysts: Geometric and Electronic from Advanced X-Ray Spectroscopies and Computational Studies. *ChemCatChem* **2020**, *12*, 1325-1333.

(101) Li, H.; Evans, E. J.; Mullins, C. B.; Henkelman, G. Ethanol Decomposition on Pd-Au Alloy Catalysts. *J. Phys. Chem. C* **2018**, *122*, 22024-22032.

(102) Hannagan, R. T.; Giannakakis, G.; Flytzani-Stephanopoulos, M.; Sykes, E. C. H. Single-Atom Alloy Catalysis. *Chem. Rev.* **2020**, *120*, 12044-12088.

(103) Li, H.; Chai, W.; Henkelman, G. Selectivity for Ethanol Partial Oxidation: The Unique Chemistry of Single-Atom Alloy Catalysts on Au, Ag, and Cu(111). *J. Mater. Chem. A* **2019**, *7*, 23868-23877.

(104) Patel, D. A.; Hannagan, R. T.; Kress, P. L.; Schilling, A. C.; Çinar, V.; Sykes, E. C. H. Atomic-Scale Surface Structure and CO Tolerance of NiCu Single-Atom Alloys. *J. Phys. Chem. C* **2019**, *123*, 28142-28147.

(105) Duchesne, P. N.; Li, Z. Y.; Deming, C. P.; Fung, V.; Zhao, X.; Yuan, J.; Regier, T.; Aldalbahi, A.; Almarhoon, Z.; Chen, S.; Jiang, D.-E.; Zheng, N.; Zhang, P. Golden Single-Atomic-Site Platinum Electrocatalysts. *Nat. Mater.* **2018**, 17, 1033-1039.

(106) Bader, R. F. W. *Atoms in Molecules: A Quantum Theory*; Oxford University Press: Oxford, 1990.

(107) Brown, G. *The Inaccessible Earth: An Integrated View to Its Structure and Composition*; Springer Science & Business Media: Switzerland, 2012.

(108) Lucci, F. R.; Darby, M. T.; Mattera, M. F. G.; Ivimey, C. J.; Therrien, A. J.; Michaelides, A.; Stamatakis, M.; Sykes, E. C. H. Controlling Hydrogen Activation, Spillover, and Desorption with Pd-Au Single-Atom Alloys. *J. Phys. Chem. Lett.* **2016**, *7*, 480-485.

(109) Derry, G. N.; Kern, M. E.; Worth, E. H. Recommended Values of Clean Metal Surface Work Functions. *J. Vac. Sci. Technol., A* **2015**, *33*, 060801.

(110) Tran, R.; Li, X.-G.; Montoya, J. H.; Winston, D.; Persson, K. A.; Ong, S. P. Anisotropic Work Function of Elemental Crystals. *Surf. Sci.* **2019**, *687*, 48-55.

(111) Réocreux, R.; Uhlman, M.; Thuening, T.; Kress, P.; Hannagan, R.; Stamatakis, M.; Sykes, E. C. H. Efficient and Selective Carbon-Carbon Coupling on Coke-Resistant PdAu Single-Atom Alloys. *Chem. Commun.* **2019**, *55*, 15085-15088.

(112) Kress, P.; Réocreux, R.; Hannagan, R.; Thuening, T.; Boscoboinik, J. A.; Stamatakis, M.; Sykes, E. C. H.

Mechanistic Insights into Carbon-Carbon Coupling on NiAu and PdAu Single-Atom Alloys. *J. Chem. Phys.* **2021**, *154*, 204701.

TOC Graphic